Hydrodynamic Characteristics and Geometric Properties of Plunging and Spilling Breakers over Impermeable Slopes

Mayilvahanan Alagan Chella[1]*, Hans Bihs[1], Dag Myrhaug[2], Michael Muskulus[1]
[1]Department of Civil and Environmental Engineering
[2]Department of Marine Technology
Norwegian University of Science and Technology (NTNU), 7491 Trondheim, Norway

Ocean Modelling, 2016, **103** , pp. 53-72.

Abstract

The two-phase flow CFD model REEF3D has been used for modelling waves breaking over a sloping seabed for a spilling and a plunging breaker. This model is based on Reynolds-averaged Navier-Stokes (RANS) equations with the level set method (LSM) for the free surface and $k-\omega$ model for turbulence. First, the characteristics and geometric properties of plunging breaking waves with different offshore wave steepnesses over slopes are examined and discussed. The study further explores the hydrodynamic characteristics of spilling and plunging breakers in terms of the wave height evolution and attenuation, horizontal and vertical velocity, free surface profile evolution, and the geometric properties during the development of the breaking process. The numerical results show a good agreement with experimental data in terms of free surface elevation and horizontal and vertical velocity for the spilling and plunging breakers. Results of numerical simulations describing the physical flow characteristics such as the formation of the forward overturning water jet, air pocket, splash-up, and the secondary wave during the breaking process are presented for both cases. For both cases, the physical flow process is found to have similar flow features, but the breaking process occurs at significantly different scales.

Keywords:

Breaking waves, spilling breaker, plunging breaker, hydrodynamic characteristics, sloping seabed

1 Introduction

Wave breaking is a two-phase flow process composed of air and water, which transforms the large scale deterministic irrotational flow into rotational flow resulting in turbulence and vortices of different types and scales. The wave breaking process in shallow waters naturally

*Corresponding author, mayilvahanan.a.chella@ntnu.no
Postprint, published in Ocean Modelling, doi: http://dx.doi.org/10.1016/j.ocemod.2015.11.011

influences many physical processes such as wave energy dissipation, air-sea interaction, wave-structure interaction, rip current, cross-shore and along-shore currents, sediment transport, shoreline evaluation. Breaking waves are strongly influenced by the local wave parameters and seabed slope, and are described by four different types: spilling, plunging, collapsing and surging (**?**). Breaking waves exert significant hydrodynamic loading on offshore platforms and foundations of offshore wind turbines in intermediate and shallow water. A recent feasibility study on the deployment of offshore wind turbines on Thornton bank outside the Belgian coast shows that hydrodynamic forces from plunging breaking waves govern the design criteria of a truss substructure (**?**). Understanding the breaking process remains a challenge since both measurements and simulations are extremely intricate.

? divided the surf zone from inception to broken waves into three regions: outer, inner and run-up region. In the outer region, waves undergo drastic changes in the shape and the flow features, i.e. the flow pattern changes from irrotational flow to rotational flow. As the wave propagates farther shoreward, the wave motion becomes turbulent with low frequency components leading to the formation of wave rollers in the inner region. The region closest to the shore is the run-up region. The two-dimensional effects and longitudinal variations are more pronounced when waves approach the breaking point. On the other hand, the three-dimensional effects become more significant just after breaking and the flow becomes highly turbulent where waves undergo drastic changes in the deterministic flow characteristics. Therefore, three-dimensional effects and the surface tension effects need to be considered for a better description of air entrainment during the breaking process and the turbulent flow characteristics in the surf zone. The present study focuses on the physical process up to the inner breaking region where the three-dimensional effects are minimal, i.e. the large-scale changes in the incident deterministic flow pattern. The wave breaking process primarily depends on the following parameters: local water depth (d), offshore wave steepness (H_0/L_0, where H_0 and L_0 are wave height and wave length, respectively in deep water) and sea bed slope (m). The wave characteristics and the seabed slope are key factors in determining the breaker type (**???**). **?** described the breaker types based on the surf similarity parameter ($\xi_0 = \frac{m}{\sqrt{H_0/L_0}}$), which is a function of the wave steepness in deep water (H_0/L_0) and the seabed slope (m). For $\xi_0 < 0.5$, spilling breakers develop for waves of high steepness over mild slopes with the formation of white water foam or a small overturning water jet at the wave crest. For $0.5 < \xi_0 < 3.3$ corresponding to waves of low steepness propagating over moderate seabed slopes, waves break as plunging breakers with the larger forward overturning jet at the wave crest. Surging or collapsing breakers occur for $\xi_0 > 3.3$.

Many laboratory experiments have been performed to obtain more insights into the breaking wave geometric, kinematic, dynamic and turbulent characteristics in deep and shallow waters, such as **???????**. **?** proposed steepness and asymmetry parameters from zero-downcross analysis to describe the prominent asymmetry features of a wave that approaches breaking: crest front steepness (ε), crest rear steepness (δ), the vertical asymmetry factor (λ) and the horizontal asymmetry factor (μ) as defined in Fig. 1 (a). A detailed experimental study by **???** investigated the dynamics of surf zone turbulence under waves breaking over a sloping seabed using fibre-optic laser-Doppler anemometer (LDA) technique. They addressed the basic differences in the turbulent characteristics and turbulence production mechanisms between spilling and plunging breakers. A number of studies have reviewed the wave evolution, flow properties and physical characteristics of waves breaking in deep and shallow water **?????**.

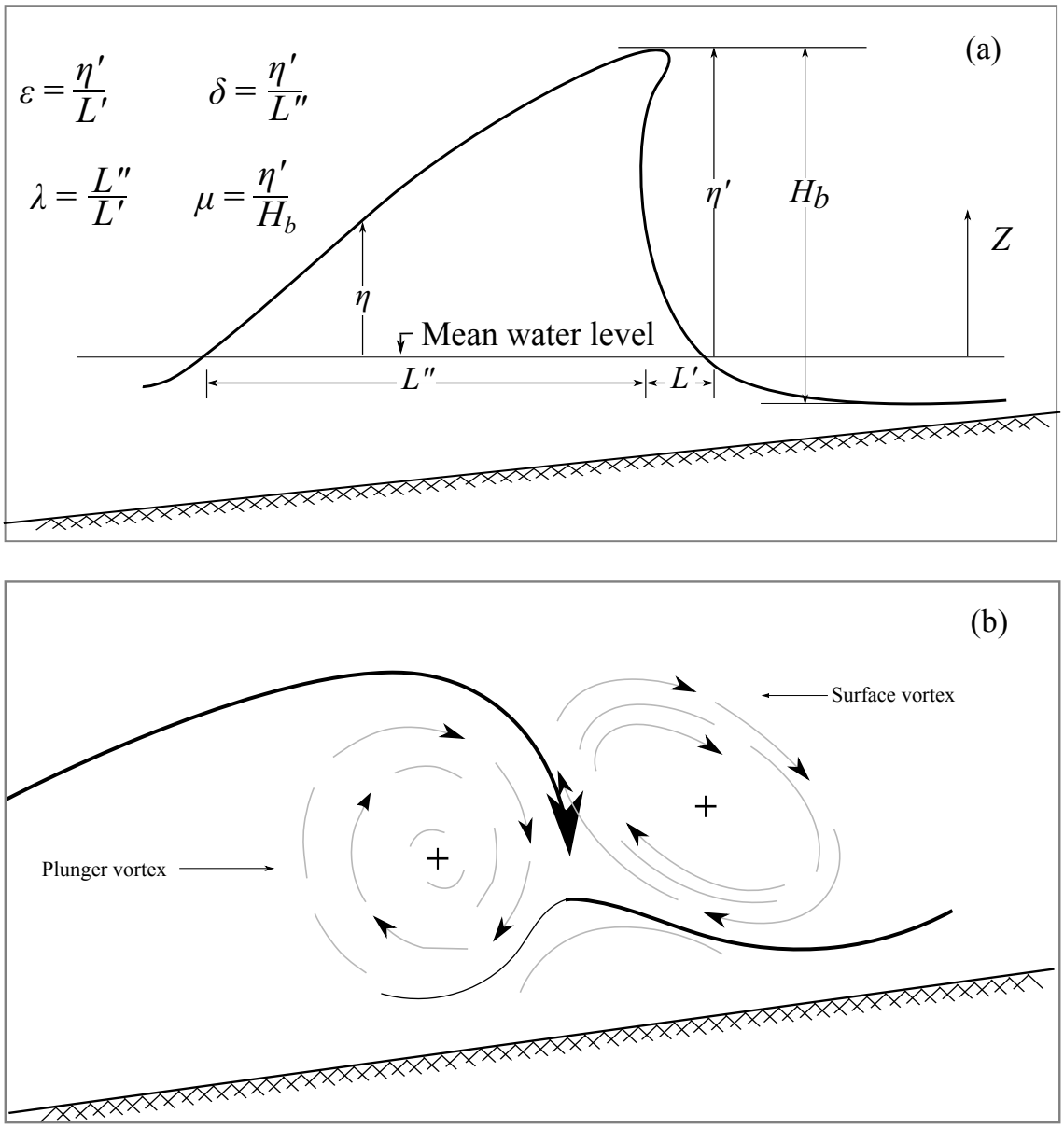

Figure 1: (a) Definition sketch of local steepness and asymmetry parameters following **?** (b) Schematic of formation of plunger vortex and surface vortex during breaking following **?**

Importantly, most numerical studies have addressed the deformation of solitary waves during the breaking process in shallow waters including **??**. Though a very few numerical studies have investigated the periodic waves breaking in shallow waters.

The wave transformation process in the surf zone is well represented by the Navier-Stokes equations and a direct solution of these equations is extremely complicated (**?**). With the advancements in the development of computational fluid dynamics (CFD), a numerical model that solves the Navier-Stokes equations coupled with a free surface capturing scheme is ca-

pable of solving the complex free surface flow problem and details of the fluid flow properties can be obtained. The first numerical investigation of free surface flows by directly solving the Navier-Stokes equations was demonstrated by **?**. A class of computational methods based on the Reynolds-averaged Navier-Stokes (RANS) equations was first proposed by **?** together with the volume-of-fluid method (VOF) and the $k-\epsilon$ turbulence model to simulate breaking waves in shallow water. Several studies attempted to model the breaking process using a single-phase flow model (**????**). The major inadequacies of the single-phase flow models to represent the complete wave breaking process are that they do not account for the air phase, the constant pressure assumption in air and the associated boundary conditions at the free surface. Therefore, this model can not represent the complex air-water interaction, which has a prominent role in the process. Hence, two-phase flow models are crucial to model the wave breaking process, such as **??????????**. **?** used the present numerical model to simulate spilling breakers over slopes. The authors compared the numerical results to the experimental data for the spilling breaker case in order to validate the numerical model. Moreover, the main aim of the study was to investigate the effects of water depth, offshore wave steepness, and beach slope on the characteristics and geometric properties of spilling breakers over slopes.
The present numerical study uses the incompressible Reynolds-Averaged Navier-Stokes equations based numerical wave tank. Unlike most of the previous numerical studies on breaking waves, in the current numerical model, different approaches have been proposed for describing the computational grid architecture and discretization schemes. The employment of the Cartesian grid facilitates to implement higher order spatial and temporal discretization schemes that provide very good numerical accuracy and stability. Particular attention has been given to achieve a more accurate representation of free surface waves in order to avoid the unrealistic damping at the free surface.
Several numerical studies that are aimed at modelling the surf zone hydrodynamics have shown quite good results, but far too little attention has been paid to investigate the evolution of the free surface profile and the prominent flow features during the breaking process. In the hydrodynamic load assessment point of view, the evolution of free surface profiles, wave height and changes in velocities and geometric properties associated with the initial breaking process are important for the modelling of breaking wave forces. Meanwhile, there have been limited studies on these hydrodynamic characteristics relevant to the load assessment parameters in shallow waters.
The main purpose of the present paper is to investigate the hydrodynamic and geometric properties of plunging breakers over slopes with the two-phase flow CFD model REEF3D and compare them with the spilling breakers (**?**). Comparison with similar results obtained for spilling breakers in **?** are also discussed. First, the study assesses the characteristics and geometric properties of plunging breaking waves of different offshore wave steepnesses over different slopes. This has been accomplished by examining the breaking characteristics such as breaker water depth (d_b), breaker depth index ($\gamma_b = H_b/d_b$, where H_b is the wave height at breaking), breaker height index ($\Omega_b = H_b/H_0$), and the profile asymmetry parameters as proposed by **?** at the breaking point. Further, the hydrodynamic characteristics during the initial breaking process over a sloping seabed are compared for both cases. This assessment has been carried out based on the wave height evolution and attenuation, horizontal and vertical velocities, free surface profile evolution, and geometric properties during the development of the breaking process.

2 Computational model

2.1 Governing Equations

The governing equations for the two-phase viscous flow in the open-source CFD model REEF3D are the incompressible Reynolds-Averaged Navier-Stokes equations:

$$\frac{\partial U_i}{\partial x_i} = 0 \tag{1}$$

$$\frac{\partial U_i}{\partial t} + U_j \frac{\partial U_i}{\partial x_j} = -\frac{1}{\rho}\frac{\partial P}{\partial x_i} + \frac{\partial}{\partial x_j}\left[(\nu + \nu_t)\left(\frac{\partial U_i}{\partial x_j} + \frac{\partial U_j}{\partial x_i}\right)\right] + g_i \tag{2}$$

U is the velocity averaged over time t, ρ is the fluid density, P is the pressure, ν is the kinematic viscosity, ν_t is the eddy viscosity and g the gravity term.

To prevent the unrealistic damping of free surface waves, higher order schemes are used in the numerical model. The fifth-order Weighted Essentially Non-Oscillatory (WENO) scheme is employed to discretize the convection term of the RANS equations (**?**). This produces numerical solutions with higher order accuracy and provides good numerical stability with non-oscillatory performance near the interface, i.e. discontinuities. In order to achieve higher order accuracy in the temporal discretization, the third-order total variation diminishing (TVD) Runge-Kutta scheme (**?**) is employed in the present study and this method includes three Euler substeps. The pressure term is treated with the projection method (**?**) after each of the Euler substeps. The Poisson equation for the pressure is solved with the BiCGStab algorithm with Jacobi preconditioning (**?**). With an adaptive time stepping method proposed by **?**, the CFL stability criterion is maintained and the simulation time step is adjusted for each iteration. This method includes the effects of velocity and the source term S on the temporal numerical solutions. In this algorithm, the time step size for each iteration is obtained by satisfying the following criterion:

$$\Delta t \leq 2\left(\left(\frac{|u|_{max}}{dx} + D\right) + \sqrt{\left(\frac{|u|_{max}}{dx} + D\right)^2 + \frac{4\,|S_{max}|}{dx}}\right)^{-1} \tag{3}$$

Which includes the effect of diffusion term D:

$$D = max\,(\nu + \nu_t) \cdot \left(\frac{2}{(dx)^2} + \frac{2}{(dy)^2} + \frac{2}{(dz)^2}\right) \tag{4}$$

Moreover, the CFL number of the present simulation cases is 0.1 and the simulations are performed at sufficiently small time steps to capture the nonlinear dynamic effects evolve during the breaking process.

The prominent features associated with the breaking process are the production, dissipation and diffusion of vorticity and turbulence. The two-equation k-ω model **?** is employed in the numerical model in order to obtain the turbulence closure for the RANS equations and the equations for k and ω as follows:

$$\frac{\partial k}{\partial t} + U_j \frac{\partial k}{\partial x_j} = \frac{\partial}{\partial x_j}\left[\left(\nu + \frac{\nu_t}{\sigma_k}\right)\frac{\partial k}{\partial x_j}\right] + P_k - \beta_k k\omega \tag{5}$$

$$\frac{\partial \omega}{\partial t} + U_j \frac{\partial \omega}{\partial x_j} = \frac{\partial}{\partial x_j}\left[\left(\nu + \frac{\nu_t}{\sigma_\omega}\right)\frac{\partial \omega}{\partial x_j}\right] + \frac{\omega}{k}\alpha P_k - \beta\omega^2 \tag{6}$$

P_k is the turbulent production rate, the coefficients have the values α=$\frac{5}{9}$ $\beta_k = \frac{9}{100}$ and β=$\frac{3}{40}$. **?** extensively investigated the performance of the $k-\omega$ turbulence model for a wide range of applications including the problems relevant to free surface flows. This model has also been applied to study the breaking waves by **?** and **?**. The $k-\omega$ model together with the RANS equations are used to model the turbulence under the breaking waves. **?** studied the spilling breakers using the Navier-Stokes equations with a $k-\omega$ turbulence model. The authors addressed that the large levels of unphysical turbulence production affect the wave propagation characteristics and this occurs in the highly strained oscillatory motion outside the boundary layer. In the present study, the unphysical turbulence production is avoided by limiting the turbulent eddy viscosity using the limiter as suggested by **?**. In the case of a two-phase flow scenario, the RANS turbulence closure over predicts the turbulence intensity at the free surface, which leads to over production of turbulence at the free surface as well. This has been controlled by implementing an additional turbulence damping scheme at the interface as proposed by **?**. The specific turbulent dissipation at the interface and the corresponding term is imposed around the interface. The solid boundaries of the fluid domain are represented with a ghost-cell immersed boundary method (**?**). The near-wall effects are accounted through wall functions for the velocities and the variables of the turbulence model.

2.2 Free surface

The interface deformation during the breaking process is complex due to the change in fluid properties such as viscosity and density across the interface. The interface deformation, i.e. free surface changes, are captured by the level set method (**?**) without explicitly tracking the interface. The interface is modeled as the zero set of the smooth signed distance function $\phi(\vec{x}, t)$ defined on the entire computational domain. The location and the sign of the zero level set function defines the fluid phase as follows:

$$\phi(\vec{x}, t) \begin{cases} > 0 \ if \ \vec{x} \in water \\ = 0 \ if \ \vec{x} \in \Gamma \\ < 0 \ if \ \vec{x} \in air \end{cases} \tag{7}$$

The free surface motion is described by the propagation of the zero level set function. The convection equation of the level set function is as follows:

$$\frac{\partial \phi}{\partial t} + U_j \frac{\partial \phi}{\partial x_j} = 0 \tag{8}$$

The Eikonal equation $|\nabla \phi| = 1$ is valid in the computational domain. In the present study, the mass conservation property is improved by reinitializing the level set function after each time step with a PDE based reinitialization equation proposed by **??**. The density and viscosity of the two phases are discontinuous at the interface. Numerical instabilities may occur due to viscosity and density jumps at the interface. This can be eliminated by smoothing out the fluid properties in a transition zone with a Heaviside function $H(\phi)$. The

thickness of the transition region is 2ϵ, where ϵ=2.1 dx. The density and the viscosity are smoothed at the interface as follows:

$$\begin{aligned} \rho(\phi) &= \rho_{water} H(\phi) + \rho_{air}(1 - H(\phi)), \\ \nu(\phi) &= \nu_{water} H(\phi) + \nu_{air}(1 - H(\phi)) \end{aligned} \tag{9}$$

and where $H(\phi)$ is a Heaviside function:

$$H(\phi) = \begin{cases} 0 & if\ \phi < -\epsilon \\ \frac{1}{2}\left(1 + \frac{\phi}{\epsilon} + \frac{1}{\pi} sin\left(\frac{\pi\phi}{\epsilon}\right)\right) & if\ |\phi| < \epsilon \\ 1 & if\ \phi > \epsilon \end{cases} \tag{10}$$

2.3 Numerical wave generation and absorption

The computational experiments are performed in a numerical wave tank. The relaxation method presented by **?** is employed for wave generation at the inlet of the numerical wave tank. Here the values for the velocities and free surface are ramped up to the values obtained from wave theory. At the outlet of the numerical wave tank, the relaxation method works as a numerical beach. Here, the velocities are set to zero, the pressure to its hydrostatic distribution and the free surface to the still water level.

3 Computational set-up and simulation cases

Breaker type	Deep water wave height, H_0 (m)	Wave period, T (s)	Experimental data			Numerical results		
			x_b(m)	H_b(m)	H/d	x_b(m)	H_b(m)	H/d
Spilling	0.127	2.0	6.40	0.165	0.78	6.28	0.172	0.775
Plunging	0.089	5.0	7.795	0.191	1.24	7.84	0.205	1.164

Table 1: Wave conditions and the experimental data in the laboratory observations by **?**; present numerical results (grid size, dx=0.005m)

Numerical experiments are conducted in a wave tank with a 1/35 sloping bed and waves are generated in the region of a flat bed of 0.4m water depth. The computational set-up follows the experimental conditions reported by **??** as shown in Fig. 2. It has been reported by **??** that cnoidal waves were used in the laboratory experiments. In order to reproduce the experimentally measured waves in the numerical simulation, three different wave theories are tested namely, shallow water cnoidal waves, first-order and fifth-order cnoidal waves. Finally, with the fifth-order cnoidal wave theory by **?**, a very good representation of the measured waves is obtained in the numerical simulation. The wave parameters that are used in the simulations are listed in Table 1. The size of the 2D computation domain is L_x=30m and L_z=1.0m. A uniform grid is used in both horizontal and vertical directions i.e. dx=dz. The length of the numerical simulation is 25s for spilling breakers and 35s for plunging breakers. The mean quantities are obtained from the simulated values of last five waves e.g. the breaker

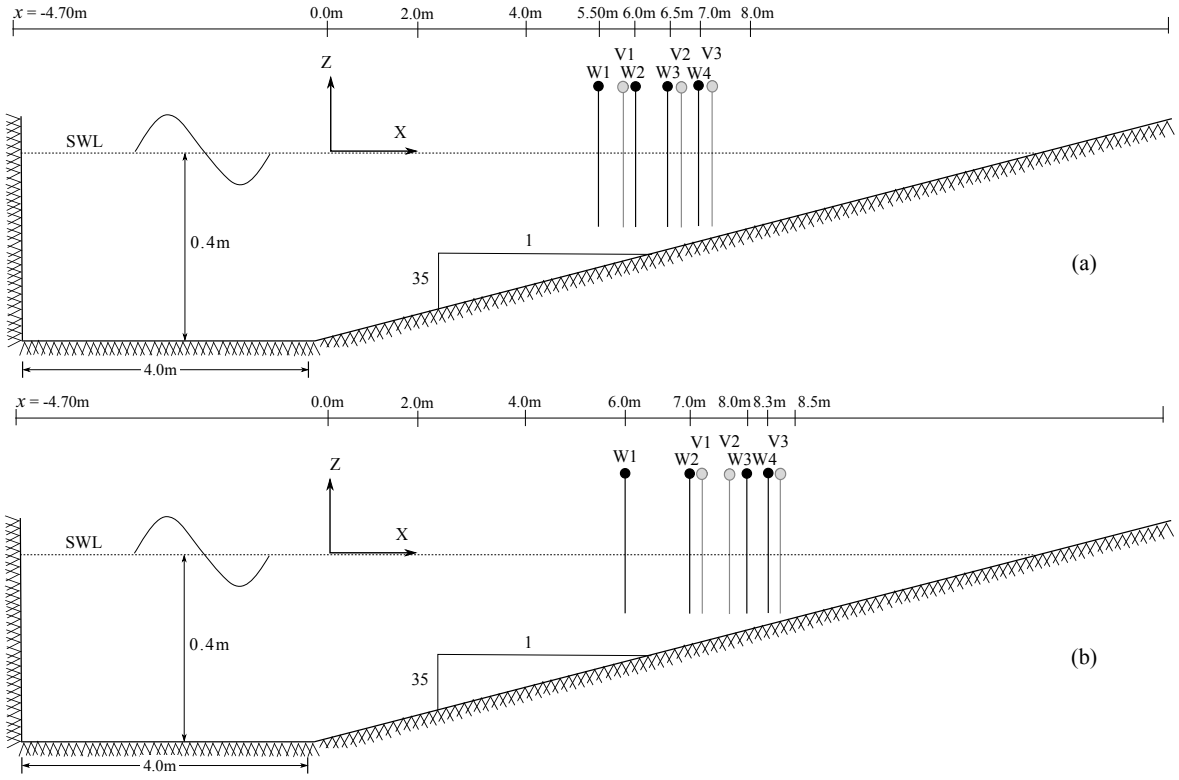

Figure 2: Computational and experimental arrangements: W1-W4 are wave gauge locations and V1-V3 are velocity probe locations for (a) the spilling case and (b) the plunging case

height (H_b) and breaking location (x_b).

In order to examine the characteristics and geometric properties of plunging breakers of different offshore wave steepness (H_0/L_0) over different slopes (m), a series of numerical experiments are performed. In the simulation cases, the environment parameters for plunging breakers are chosen based on the surf similarity parameter suggested by **?**. This also includes a few transitional spilling-plunging breakers, as listed in Table 2.

Simulation cases	Offshore wave steepness, H_0/L_0	Seabed slope, (m)	Surf similarity parameter, (ξ)
Case A	0.0023	1/15 1/25 1/35 1/45 1/55	0.84 0.72 0.60 0.50 0.42
Case B	0.0011 0.0016 0.0023 0.0035	1/35	0.84 0.72 0.60 0.49

	0.0046		0.42

Table 2: List of simulation cases

3.1 Grid sensitivity study

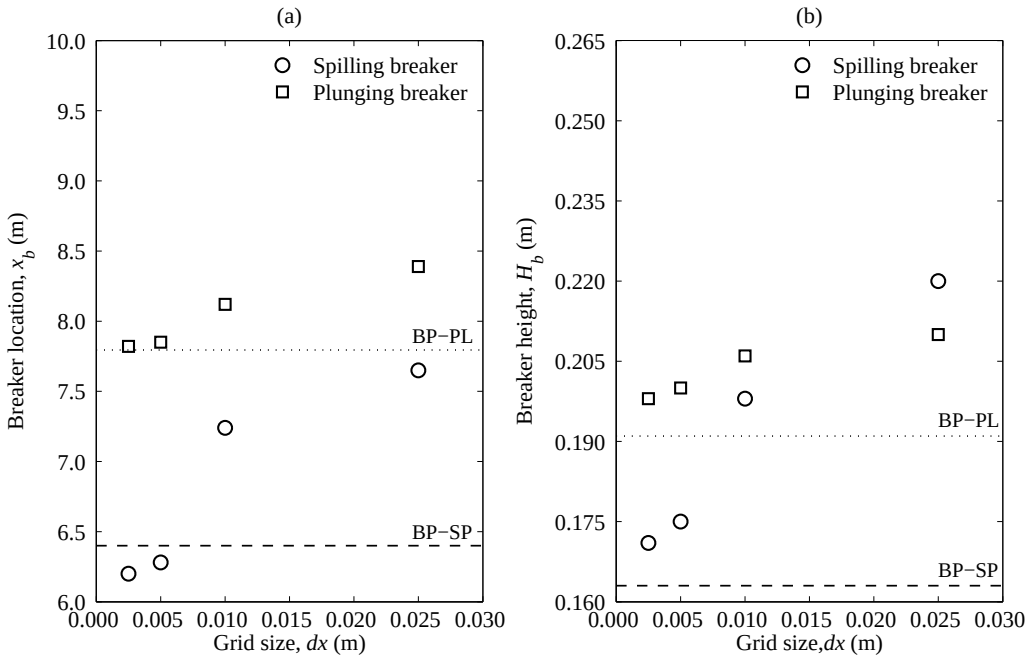

Figure 3: Comparison of (a) x_b and (b) H_b for different grid sizes. BP-SP and BP-PL are the measured data by **??** for the spilling and plunging breaker, respectively.

The sensitivity of the numerical results to the grid size (dx) is tested with four different grid sizes, dx=0.025m, 0.01m, 0.005m and 0.0025m. Fig. 3 presents the comparison of the numerical breaking location (x_b) (Fig. 3 (a)) and the breaker height (H_b) (Fig. 3 (b)) for different grid sizes for spilling and plunging breakers. It appears that the numerical waves on coarser grids (dx=0.025m and dx=0.01m) break later and further up in the wave tank with larger breaker height than the experimental waves. On the other hand, the numerical waves on finer grids (dx=0.005m and dx=0.0025m) break at about the same location as that of the experimental waves for both cases. The numerical results at the breaking point on the grid size dx=0.005 match well with the experimental data as presented in Table 1. In addition, the difference between the results of two fine grid sizes (dx=0.005m and dx=0.0025m) is very small. Therefore, the grid size dx=0.005 is considered for the simulations.

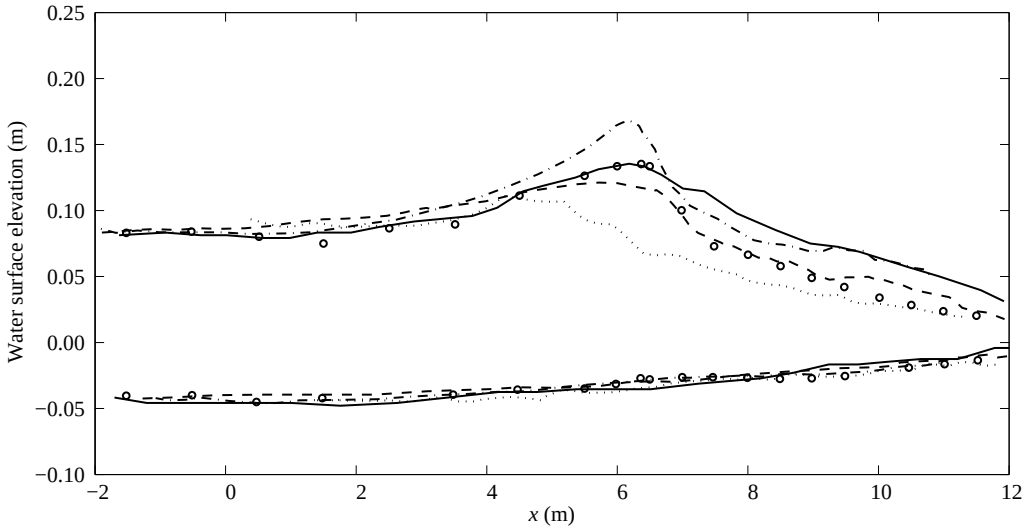

Figure 4: Comparison of the computed and measured maximum (upper curves) and minimum (lower curves) wave surface elevation for the spilling breaker. Solid lines: the present numerical model; circles: experimental data from Ting and Kirby (1996); dotted lines, numerical: Bradford (2000); dashed lines, numerical: Xie (2013); dashed-dotted lines, numerical: Zhao et al. (2004)

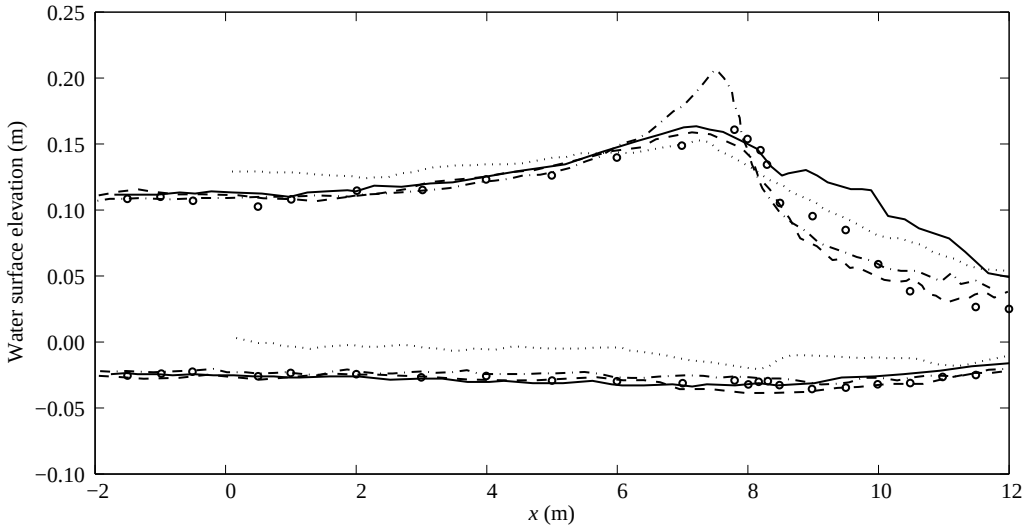

Figure 5: Comparison of the computed and maximum (upper curves) and minimum (lower curves) wave surface elevation for the plunging breaker. Solid lines: the present numerical model; circles: experimental data from Ting and Kirby (1996); dotted lines, numerical: Bradford (2000); dashed lines, numerical: Xie (2013); dashed-dotted lines, numerical: Zhao et al. (2004)

4 Results and discussion

4.1 Wave envelope of spilling and plunging breaker

Figs. 4 and 5 show the comparison of computed and measured maximum (upper curves) and minimum (lower curves) wave surface elevations for the spilling breaker and plunging breaker, respectively. The numerical results of **???** are also presented for comparison as reported in **?**. The computed results of all the numerical models show the same trend as the experimental measurements. The numerical model by **?** is a two-phase flow model based on the RANS equations together with $k-\epsilon$ and the VOF method. **?** performed simulations with the commercial software FLOW-3D that uses the RANS equations together with the VOF method and the RNG (Re-Normalized Group) turbulence model. **?** used a model based on the space filtered Navier-Stokes equations with the VOF method and the multi-scale turbulence model. In the spilling breaker case, the computed maximum and minimum wave surface elevations are quite well captured up to the breaking point by the present numerical model and the model by **?**. **?** overestimates the wave crest significantly near the breaking point and slightly in the surf zone, whereas **?** largely underestimates the wave crest near the breaking point and estimates it reasonably well in the surf zone. The comparison of computed and measured envelope of the water surface elevation for the spilling breaker is also presented in Fig. 8 of Alagan Chella et al. (2015a) using the present numerical model.

For the plunging breaker (Fig. 5), **?** overpredicts the wave crest height close to the breaking point, but predicts the wave surface quite well in the shoaling and surf zones. The numerical results by **?** show a slight overestimation of the wave crest and a significant underestimation of the wave trough. **?** shows a good comparison with the experimental data for the whole domain for both the breakers. The present numerical model shows a good representation of the wave height evolution during the shoaling and initial breaking region for both cases, but overestimates slightly the wave crest heights after the breaking point in the surf zone. However, the computed wave troughs are in a good agreement with the experimental data. The overprediction of the wave crest heights after breaking is due to the slower dissipation process in the numerical simulation.

4.2 Plunging breakers over slopes

4.2.1 Breaking process

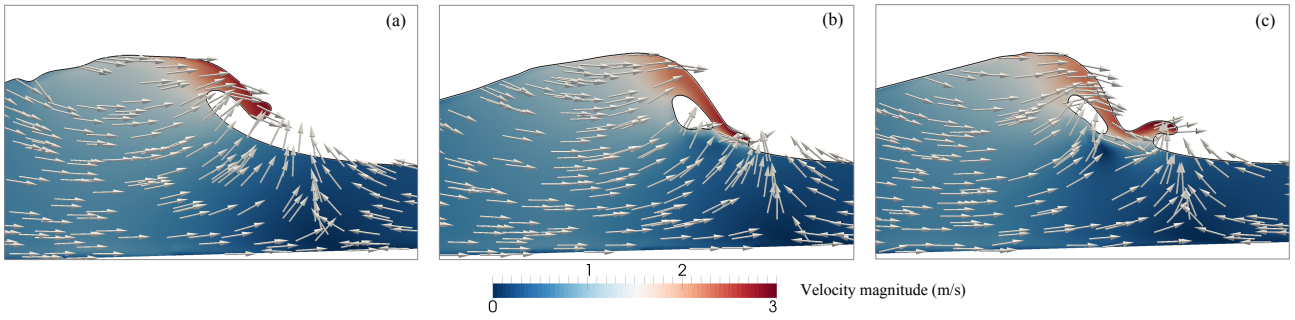

Figure 6: Wave surface profile with velocity vectors and velocity magnitude for the plunging breaker

Fig. 6 illustrates the free surface profile evolution with the velocity vectors and their magnitudes variation during the breaking process. The overturning water jet that evolves from the wave crest when the particle velocity becomes larger than the wave celerity is shown in Fig. 6 (a). The overturning wave crest then hits the free surface of the preceding wave Fig. 6 (b) and the splash-up occurs. Further, this leads to the formation of the secondary wave with new flow characteristics which depends on the size of the overturning crest as seen in Fig. 6 (c).

4.2.2 Characteristics and geometric properties

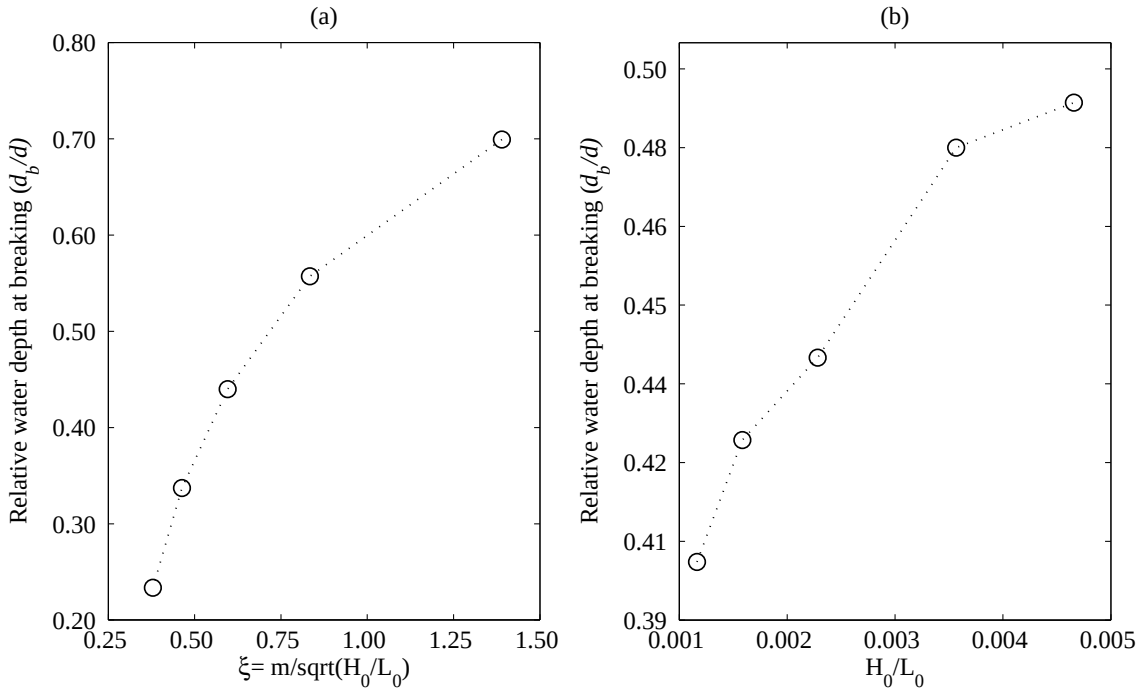

Figure 7: Numerical relative water depth (d_b/d) for different (a) surf similarity parameter ($\xi = \frac{m}{\sqrt{H_0/L_0}}$) and (b) offshore wave steepness (H_0/L_0)

Fig. 7 presents the numerical relative breaker depth (d_b/d) versus the surf similarity parameters ($\xi = \frac{m}{\sqrt{H_0/L_0}}$) (7 (a)) (since H_0/L_0 is constant) for different slopes and offshore wave steepness (H_0/L_0) (7 (b)). It appears that d_b/d increases as ξ (Fig. 7 (a)) and H_0/L_0 (Fig. 7 (b) increase. Waves break offshore at larger water depths over steeper slopes and also waves with larger wave steepeness.

Figs. 8 and **??** show the breaker depth index ($\gamma_b = H_b/d_b$) and breaker height index ($\Omega_b = H_b/H_0$) versus the surf similarity parameters (ξ) (Fig. 8) (since H_0/L_0 is constant) for different slopes and offshore wave steepness (H_0/L_0) (Fig. **??**). It appears that γ_b and Ω_b decrease as ξ and H_0/L_0 increase. Waves over milder slopes break farther onshore at shallower water depths with larger H_b as the waves deform more during the shoaling process, corresponding to ξ=0.381, d_b/d=0.233 (Fig. 7 (a)), γ_b=2.50 (Fig. 8 (a)) and Ω_b=2.60 (Fig. 8 (b)). In the case of waves over a steeper slope, breaking occurs farther offshore with a lower

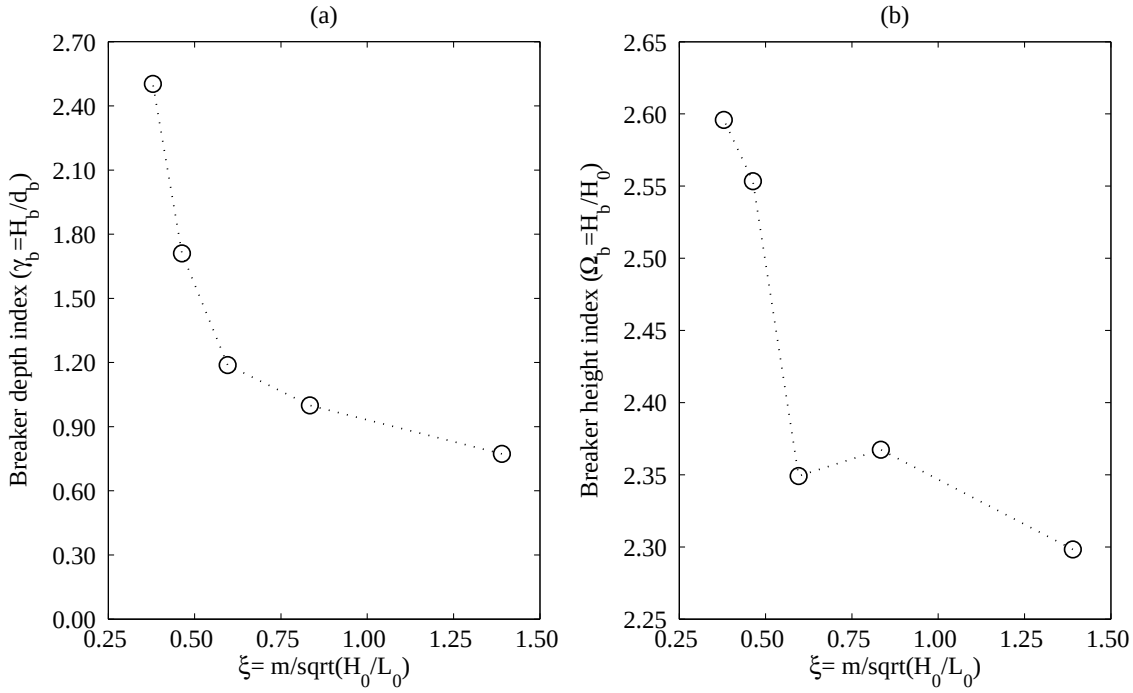

Figure 8: Numerical (a) breaker depth index ($\gamma_b = H_b/d_b$) and (b) breaker height index ($\Omega_b = H_b/H_0$) for different surf similarity parameter ($\xi = \frac{m}{\sqrt{H_0/L_0}}$)

H_b, with more partial reflections from the slope, corresponding to ξ=1.396, d_b/d=0.70 (Fig. 7 (a)), γ_b=0.77 (Fig. 8 (a)) and Ω_b=2.30 (Fig. 8 (b)). Unlike the variation of Ω_b for the spilling breaking waves with low H_0/L_0 over slopes (**?**), Ω_b decreases as the seabed slope increases for the plunging breaker. In the present case, the plunging breaking waves are relatively long waves compared to the spilling breaking waves. The plunging breakers have a deeper wave base, propagate faster, interact more with the slope and break sooner. Waves with lower H_0/L_0 break farther shoreward at shallower water with higher H_b, transform more during the shoaling process, corresponding to H_0/L_0=0.0011, d_b/d=0.40 (Fig. 7 (b)), γ_b=1.69 (Fig. **??** (a)) and Ω_b=3.04 (Fig. **??** (b)). The variation of the breaker indices versus H_0/L_0 for the plunging breakers are consistent with those for the spilling breakers as shown in Fig. 15 (b) of **?**.

Fig. 9 shows the changes in the wave profile during the breaking for different combinations of slopes and offshore wave steepnesses. Figs. 10 and 11 show the wave asymmetry parameters versus the surf similarity parameters (ξ) (Fig. 10) (since H_0/L_0 is constant) for different slopes and offshore wave steepness (H_0/L_0) (Fig. 11). It appears that ε and λ increase and μ decreases slightly ξ increases, while δ nearly constant. When the waves approach breaking over steeper slopes, the front part of the wave becomes steeper without any change in the rear crest steepness and deforms both in vertical and horizontal direction with a shallower trough and an overturning crest (Fig. 9 (a) and (b)), according to ξ=1.39, ε=1.19, μ=0.72 (Fig. 10 (a)) and λ=15.15 (Fig. 10 (b)). In spite of that both spilling and plunging breakers are found to have similar geometrical features in terms of ε, λ and μ, the rear part of the wave crest

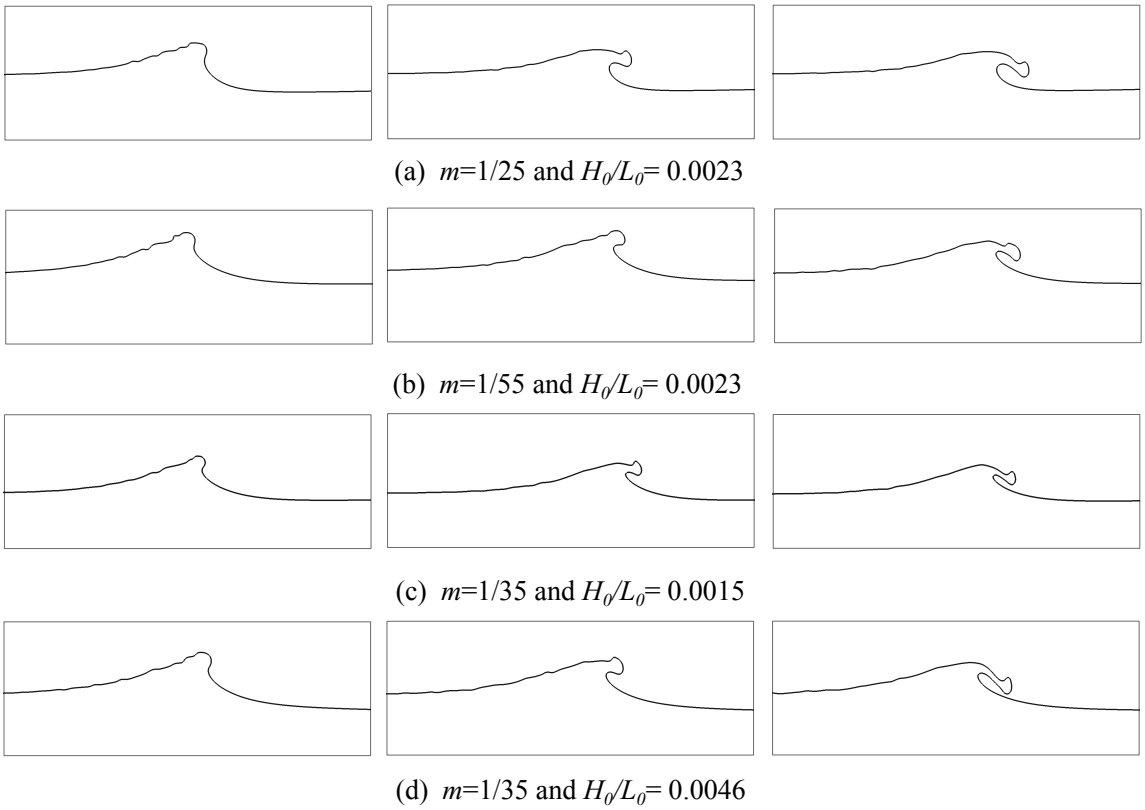

Figure 9: Computed wave profiles (a) m=1/25 and H_0/L_0=0.0023, (b) m=1/55 and H_0/L_0=0.0023, (c) m=1/35 and H_0/L_0=0.0015 and (d) m=1/35 and H_0/L_0=0.0046

does not deform during the interaction with slopes for plunging breakers.

For the waves with larger H_0/L_0 over a given slope, ε and δ increase and λ decreases as H_0/L_0 increases. This implies that the wave front and rear part become steeper without much change in the horizontal and vertical asymmetry. For the waves with lower H_0/L_0 at the breaking point, the rear part of the wave crest becomes wider and smooth with a slightly steeper front part and shallower wave trough (Fig. 9 (c) and (d), corresponding to H_0/L_0=0.0011, ε=0.73 (Fig. 11 (a)) and λ=12.96 (Fig. 11 (b)). The variation of the crest front steepness (ε) and the vertical asymmetry factor (λ) for the plunging breakers are consistent with those for the spilling breakers. However, for plunging breakers, the crest rear steepness (δ) and horizontal asymmetry factor (μ) are nearly independent of H_0/L_0.

In contrast to the previous results for spilling breakers over slopes (**?**), the wave profiles during the breaking do not change much for plunging breakers with different H_0/L_0 over slopes as shown in Fig. 9. However, the computed plunging breaking wave profiles show significant changes in the wave crest front steepness (ε) and vertical asymmetry factor (λ). Though the breaker indices exhibit a similar trend for steeper slopes and waves with larger H_0/L_0, the vertical (λ) and horizontal asymmetry (μ) of the breaking wave profiles show an opposite relationship between H_0/L_0 and steeper slopes. This confirms that the breaking mechanism has distinct geometrical features based on seabed slope and H_0/L_0.

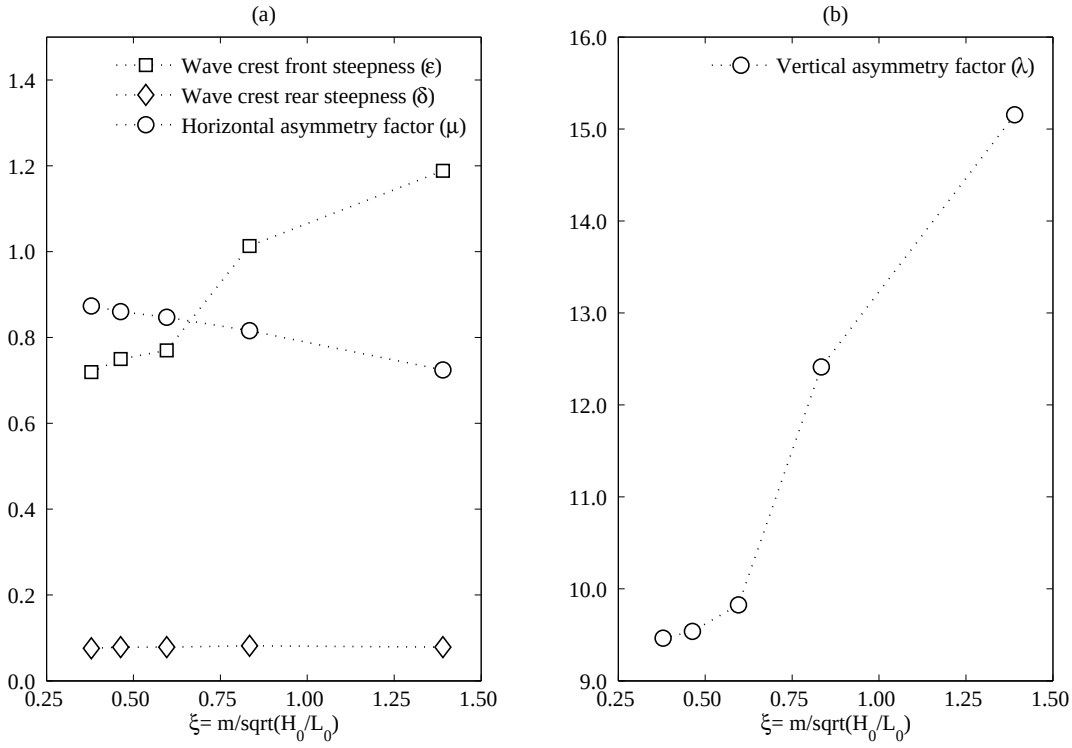

Figure 10: Numerical wave profile steepnesses and asymmetry factors for different surf similarity parameter ($\xi = \frac{m}{\sqrt{H_0/L_0}}$)

4.3 Comparison of hydrodynamic characteristics of spilling and plunging breakers over a sloping seabed

4.3.1 Free surface evaluation

Fig. 12 shows the comparison of the numerical wave surface elevations with the experimental data for the plunging breakers. When the waves propagate over the slope, the wave length and the wave speed are both reduced with decreasing water depth. Consequently, the kinetic wave energy decreases as the waves approach the shore, giving an increased potential energy, and therefore the wave height increases until breaking. The upper part of the wave tends to move faster than the lower part of the wave, resulting in the wave steepening as shown in Fig. 12 (b). A further increase in the wave height results in a significantly steeper wave profile and finally the wave breaks. As the breaking wave approaches the shore, the potential energy and the wave height decreases. A decrease in the wave height in the inner breaking region due to energy dissipation by wave breaking leads to the changes in the wave characteristics as shown in Fig. 12 (d). It should be noted that breaking occurred between Figs. 12 (c) and (d) for the plunging breaker. The computed wave surface elevations for the spilling breaker from the results of previous study by (**?**) (Fig. 4) show a similar variation trend as the plunging breaker. The numerical wave surface elevations appear to agree well with the experimental

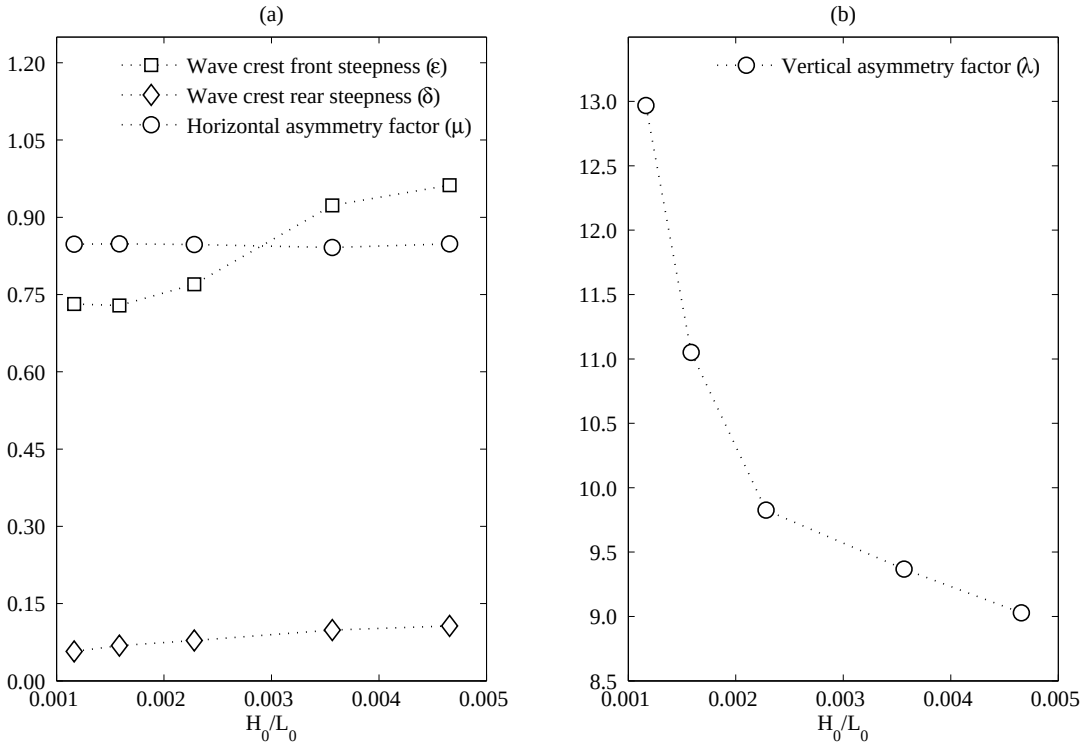

Figure 11: Numerical wave profile steepnesses asymmetry factors for different offshore wave steepness (H_0/L_0)

data by **??**. The wave height to water depth ratio H/d at wave breaking is a key parameter related to the surf zone turbulence, and it is also useful in categorizing different types of breakers in shallow water **?**. The computed H/d at the breaking is 1.164 for the plunging breaker, whereas it is 0.775 for the spilling breaker. This implies that plunging breaking occurs farther up on the slope at shallower water depths with larger breaker heights, while spilling breaking occurs farther offshore at larger water depths with a small increase in the breaker height. The computed H/d ratio for both cases are consistent with the experiments and are listed in Table 1.

4.3.2 Wave height evolution and attenuation

Fig. 13 shows the wave height variation before breaking (H/H_0) and after breaking (H/H_b) versus the non-dimensional breaking location ($\hat{x} = x/L$, x=0 at 0.7m from the toe of the slope and $x = L$ at the shoreline). As can be seen from Fig. 13 (a), the plunging breaker undergoes more deformation during shoaling as it advances over the slope than the spilling breaker. Since the plunging breaker has a deeper wave base, it feels the influence of the bed earlier. This intensifies the water particle interaction with the slope, resulting in a larger deformation. The wave height grows over the slope due to the higher shoaling rate and reaches a maximum height of $2.30H_0$ for the plunging breaker. For the spilling breaker it increases less and attains the maximum wave height at the breaking point with $1.35H_0$. Therefore, the initial wave characteristics of the wave approaching over the slope, change significantly for

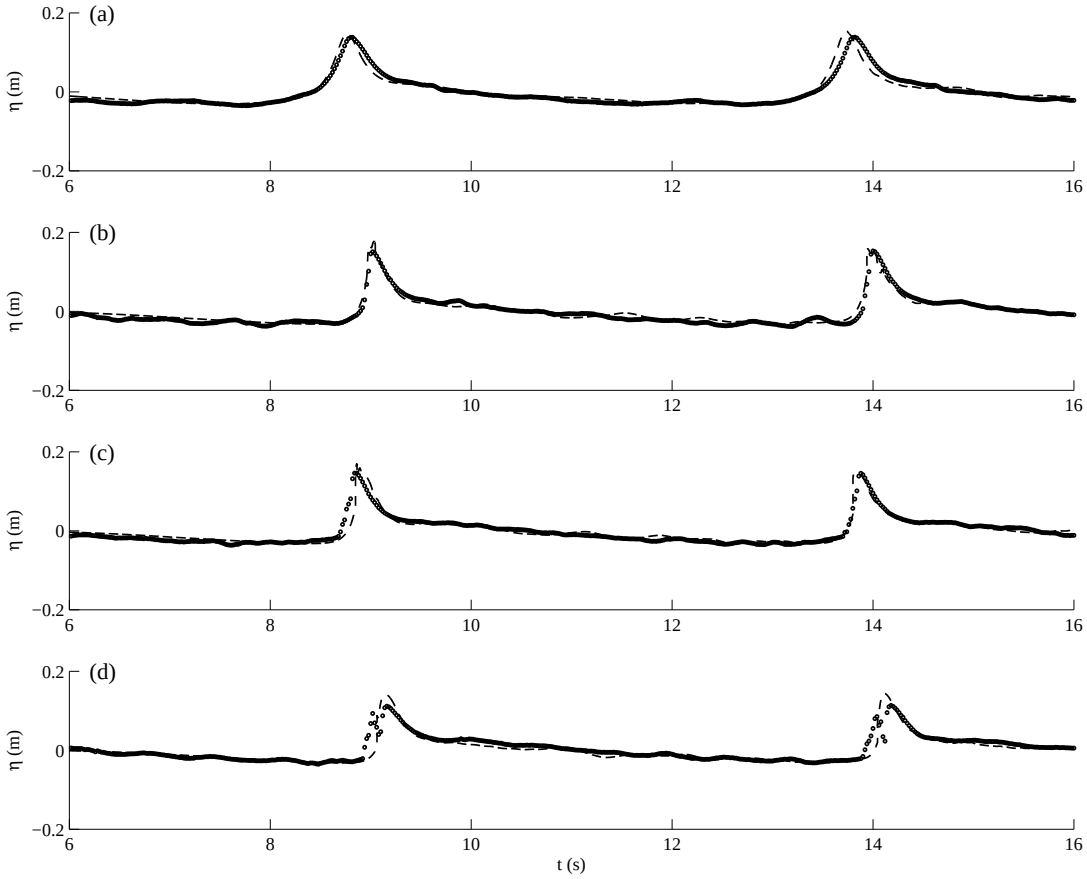

Figure 12: Comparison of numerical and experimental instantaneous wave surface elevation for the plunging breaker at x=6.0m (a), 7.0m (b), 8.0m (c) and 8.3m (d). Dashed lines: present numerical results; circles/full line: experimental results by **?**

the plunging breaker due to a deeper wave base and the higher shoaling rate.

From Fig. 13 (b) it appears that the wave height decreases gradually after breaking for the spilling breaker, whereas a more rapid wave height variation occurs for the plunging breaker which is consistent with the observations by **??** and **?**. This implies that the potential wave energy decreases gradually for the spilling breaker and rapidly for the plunging breaker in the surf zone by converting some of the potential energy into the kinetic energy plus dissipation by turbulence and bed friction. It is also possible to infer that the amount of energy generated from the plunging breaker is higher and dissipates faster than for the spilling breaker. However, the wave height decreases continuously shoreward as most of the wave energy is dissipated during the shoaling and breaking process.

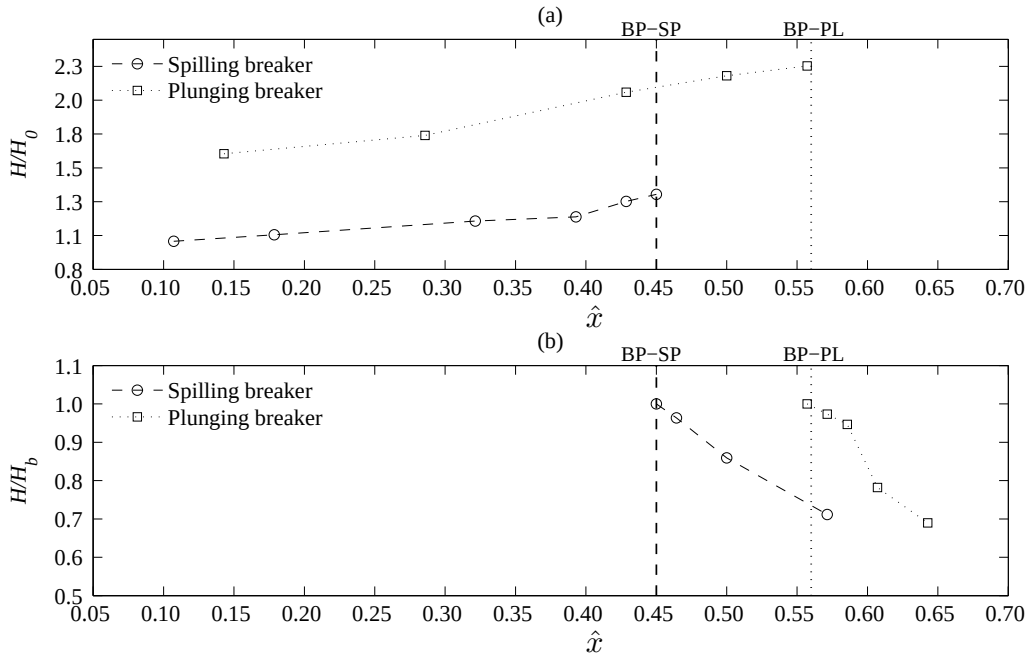

Figure 13: Computed wave height variation (a) H/H_0 (before breaking) (b) H/H_b (after breaking) versus the non-dimensional breaking location ($\hat{x}$). BP-SP and BP-PL are the breaking points for the spilling and plunging breaker, respectively.

4.3.3 Horizontal and vertical particle velocity

Figs. 14 and 15 show the comparison of the computed horizontal velocity with the experimental data at three different horizontal locations: before breaking (a), during breaking (b) and after breaking (c), at two elevations; near the free surface and close to the bed. It appears that the horizontal velocity increases shoreward until breaking, with lower velocities at the bed . The phase lag between the top and bottom velocity profile indicates that the motion of water particles close to the sloping bottom is restricted by friction during the shoaling and the breaking process. For both cases, the horizontal velocity depends on the change of the water surface level during the propagation of the wave train. The horizontal velocity distribution under the spilling and plunging breakers is presented in Figs. 16 and 17, respectively. It appears that the variation of the horizontal velocity below the trough of the plunging breaker is almost constant over the depth, but it is changing under the spilling breaker. This is also consistent with the laboratory study by **?**. Moreover, the maximum horizontal velocity occurs at the tip of the crest where potential energy is converted into kinetic energy with the formation of the horizontal surface roller. The same type of behavior is also observed during the formation of secondary wave during the splash-up phase as shown in Figs. 16 (c) and 17 (c).

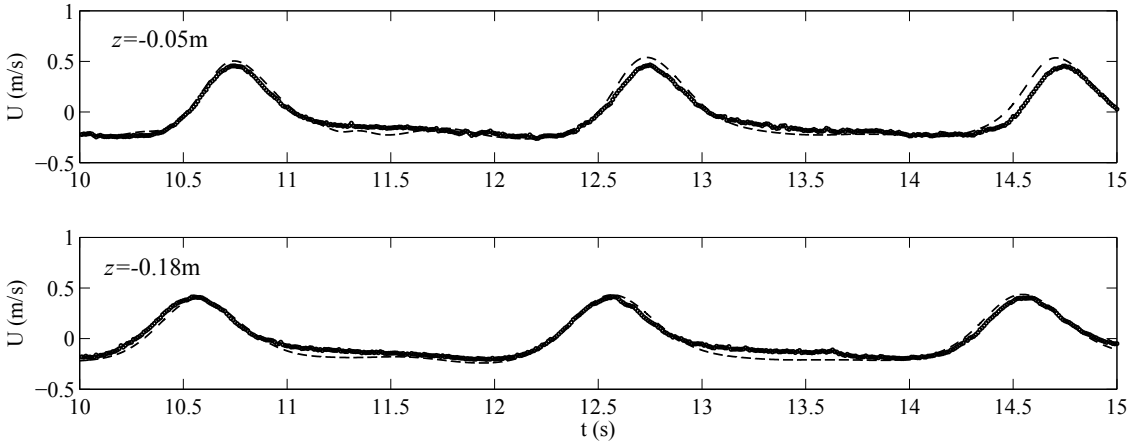

(a) x=5.945m (before breaking)

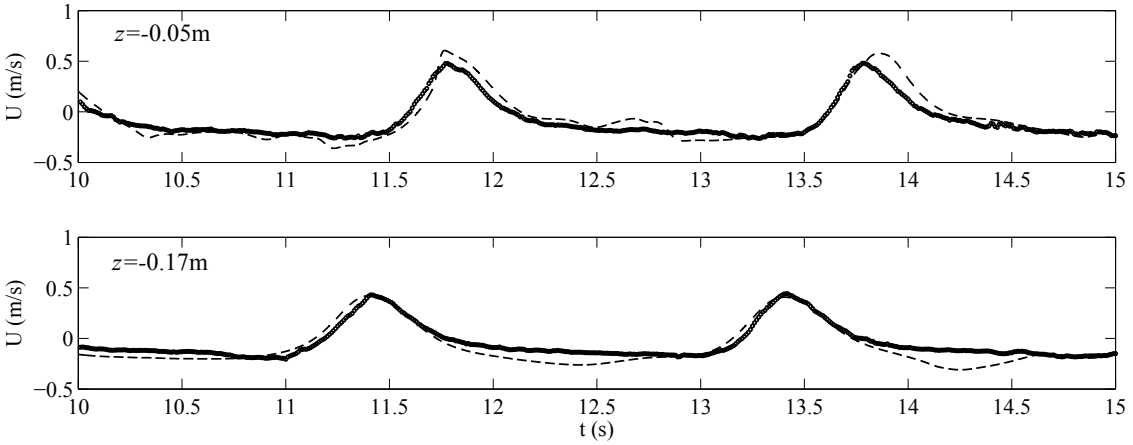

(b) x=6.665m (during breaking)

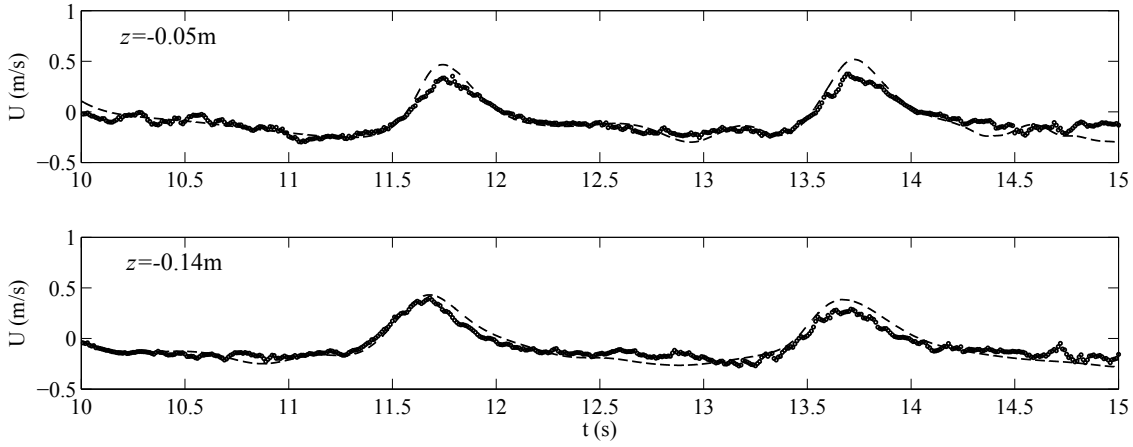

(c) x=7.275m (after breaking)

Figure 14: Comparison of numerical and experimental horizontal velocity for the spilling breaker. Dashed lines: present numerical results; circles/full line: experimental results by **?**

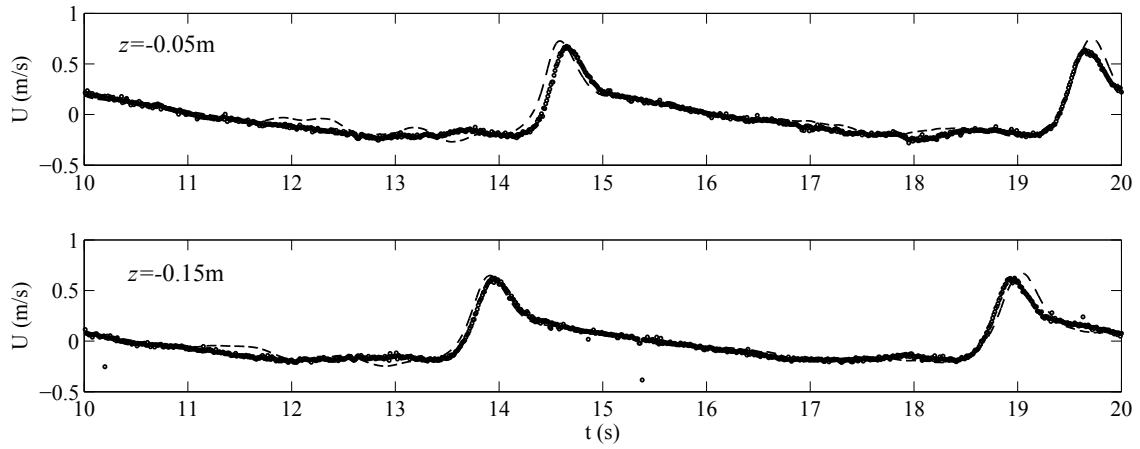

(a) x=7.295m (before breaking)

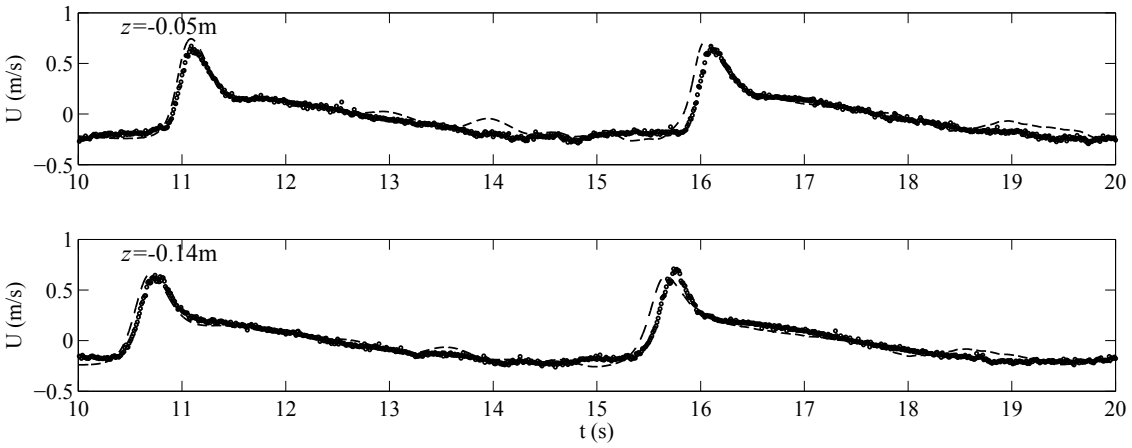

(b) x=7.725m (during breaking)

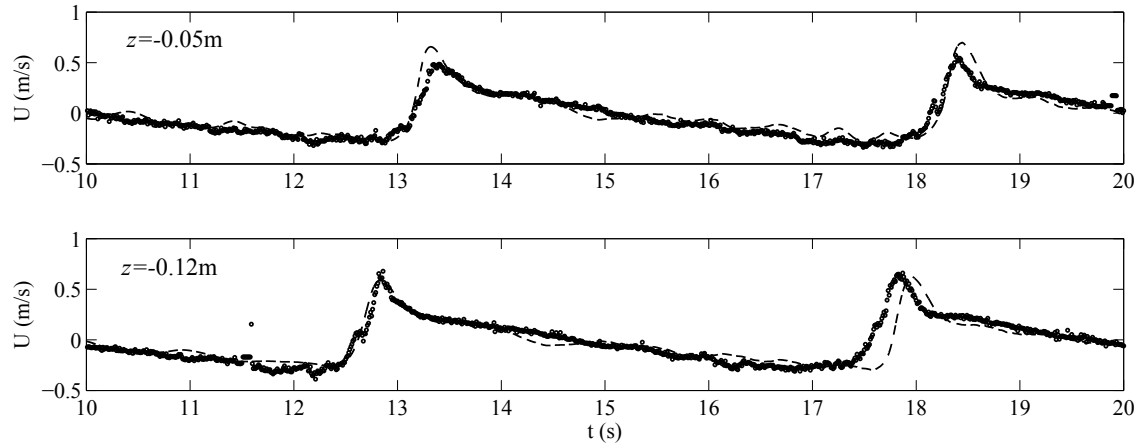

(c) x=8.345m (after breaking)

Figure 15: Comparison of numerical and experimental horizontal velocity for the plunging breaker. Dashed lines: present numerical results; circles/full line: experimental results by **?**

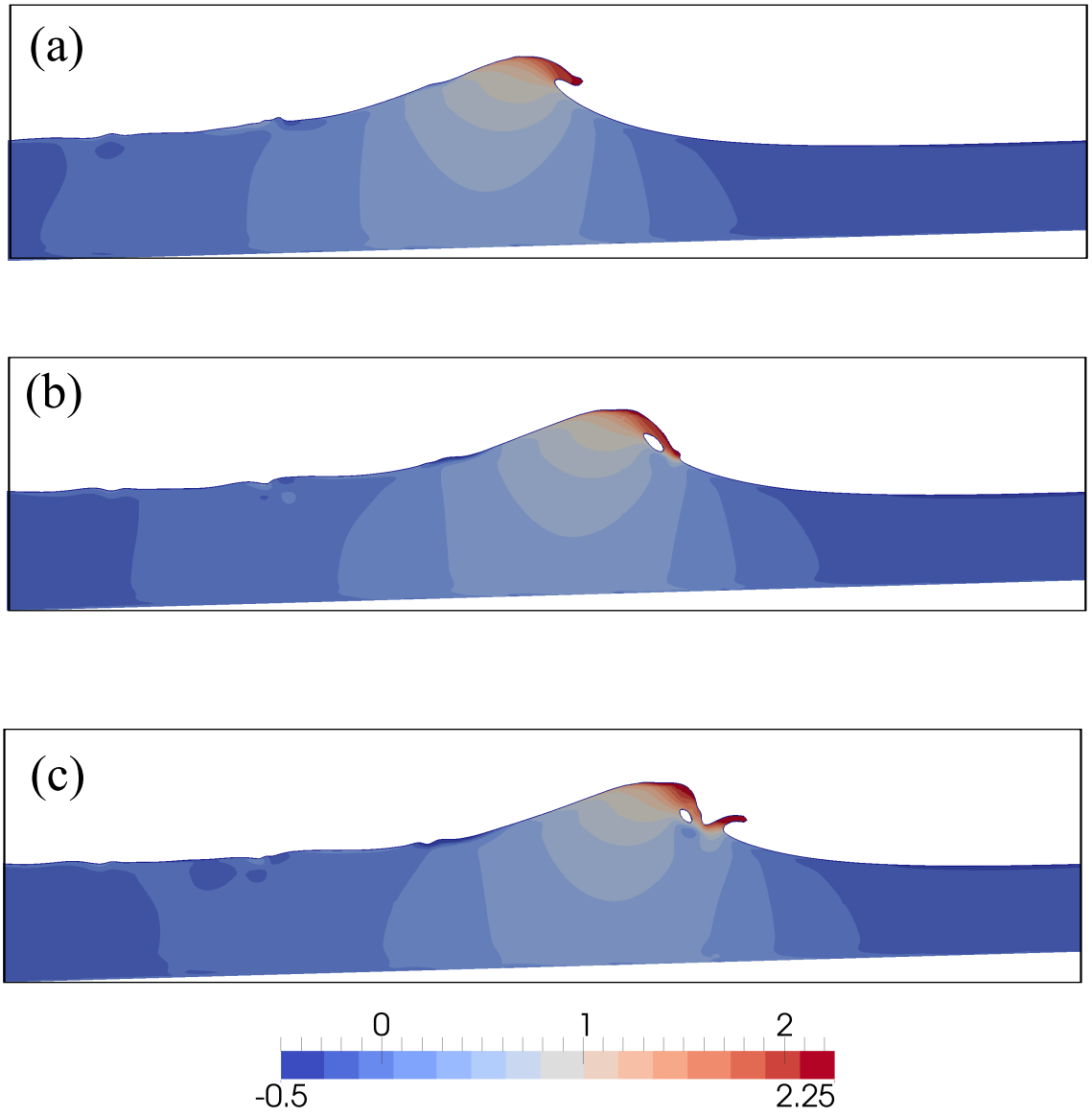

Figure 16: Variation of horizontal velocity, V_x (m/s) under the spilling breaker at t= 10.35s (a), 10.45s (b) and 10.50s (c)

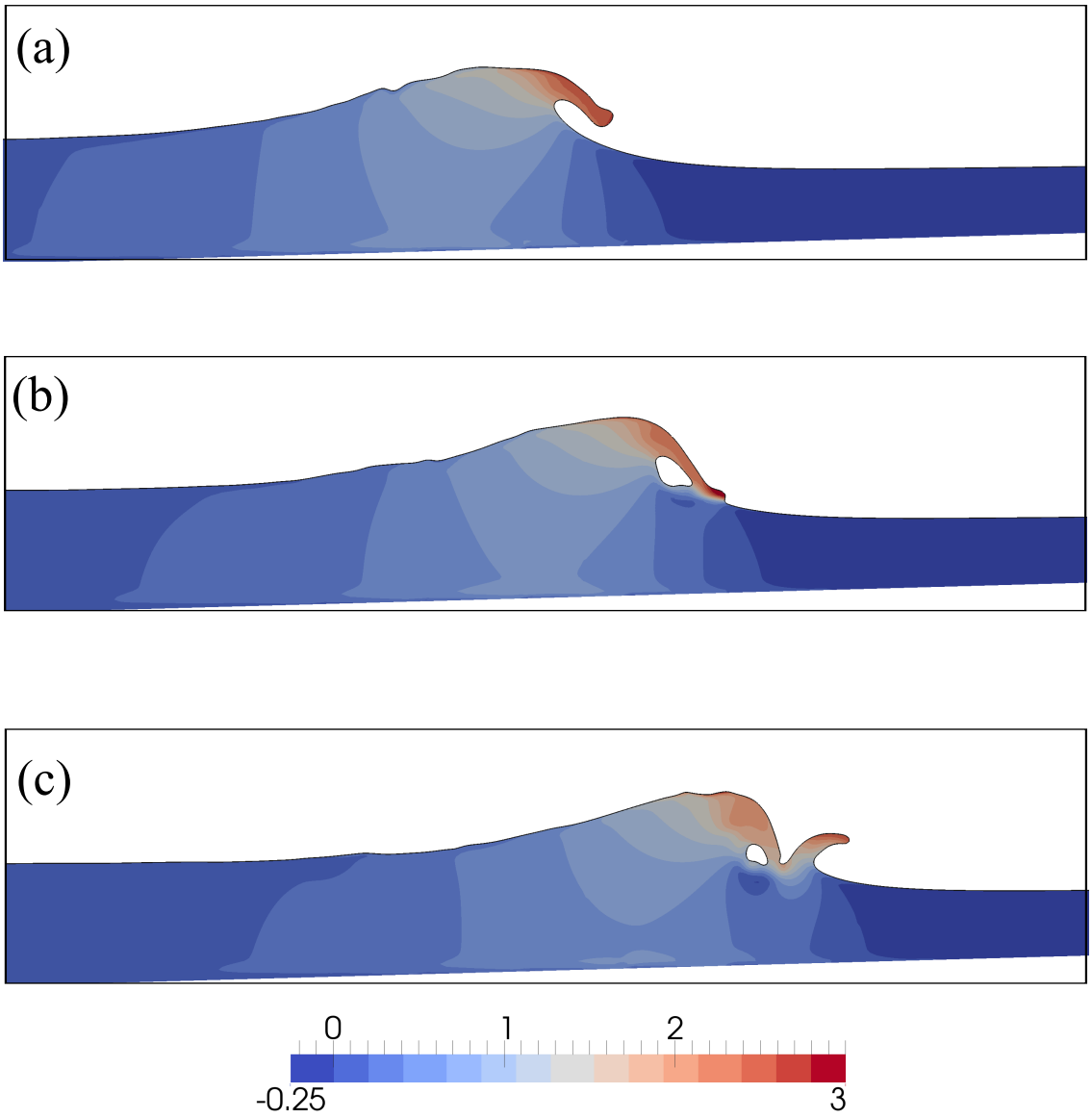

Figure 17: Variation of horizontal velocity, V_x (m/s) under the plunging breaker at t= 10.85s (a), 10.95s (b) and 11.05s (c)

Figs. 18 and 19 show the comparison of the computed vertical velocity near the free surface with the experimental data at three different horizontal locations: before breaking (a), during breaking (b) and after breaking (c). The computed vertical velocity agrees well with the measurements, though it is slightly higher than the experimental data in the outer region of the surf zone for the spilling breaker. A slight increase in the vertical particle velocity can be expected during the formation of small (spilling) and large (plunging) overturning water jets at the wave crest and the splash-up for both the breakers. For the spilling breaker, a slight

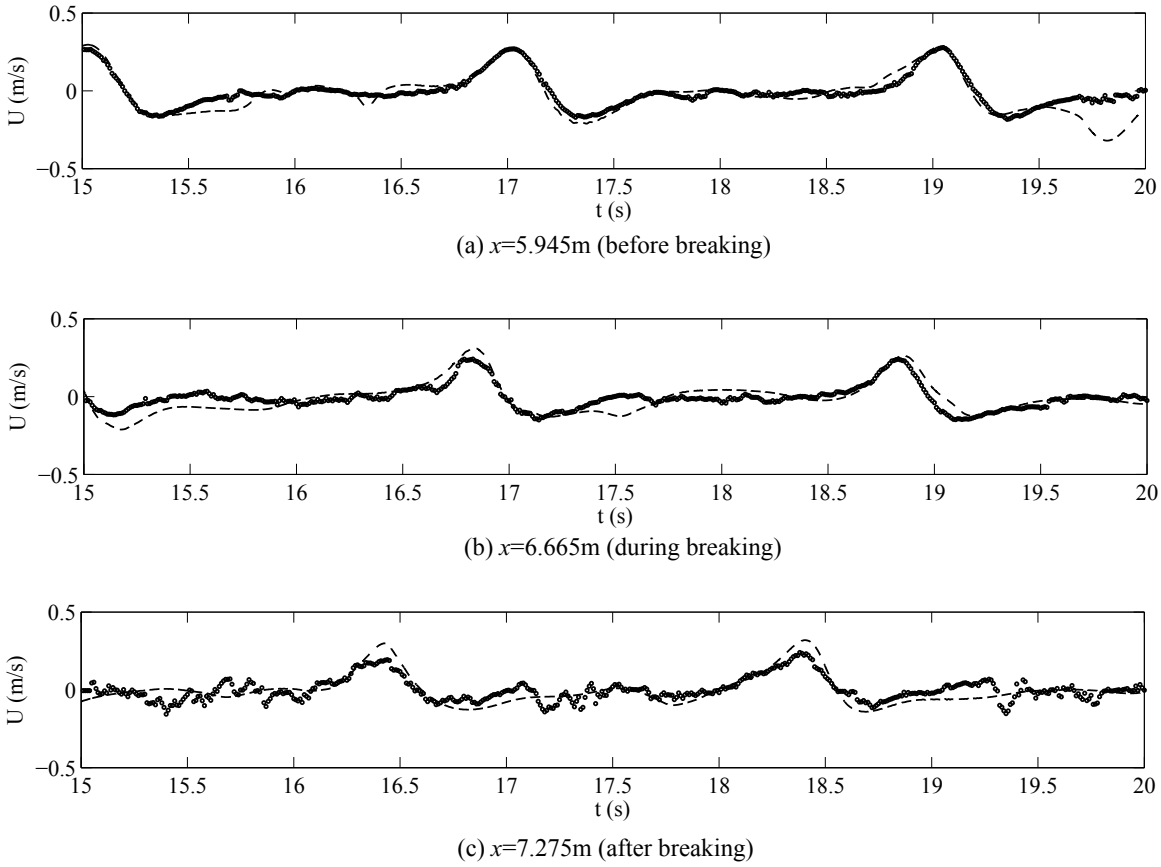

Figure 18: Comparison of numerical and experimental vertical velocity for the spilling breaker. Dashed lines: present numerical results; circles/full line: experimental results by **?**

decrease in the vertical particle velocity near the free surface is observed during the wave breaking. This is due to a stagnation phase in the flow field during the development process of the vertical wave front of the horizontal water jet. This type of behaviour is also reported by **?**. However, the computed vertical velocity clearly follows the experimental trend and it increases continuously until the formation of the secondary wave, while it decreases shoreward for the plunging breaker. Figs. 20 and 21 show the vertical velocity variation during the wave breaking process for the spilling and plunging breaker, respectively. It appears that the vertical particle velocity attains the maximum value at the mean water level near the forward portion of the wave crest. It is evident from the Figs. 20 and 21 that the maximum vertical component of velocity moves along the wave front of the propagating wave and becomes larger under the steep wave front. This is also seen in the laboratory experiment by **??**. By comparing Figs. 16 and 20 as well as Figs. 17 and 21, it appears that the velocity distribution at the overturning water jet is dominated by the horizontal velocity component with a small vertical velocity component. Although the kinematics of the secondary wave, that evolves during the splash-up, are still dominated by the horizontal velocity component, the vertical velocity component has a significant contribution in the region as shown in Figs. 20 (c) and

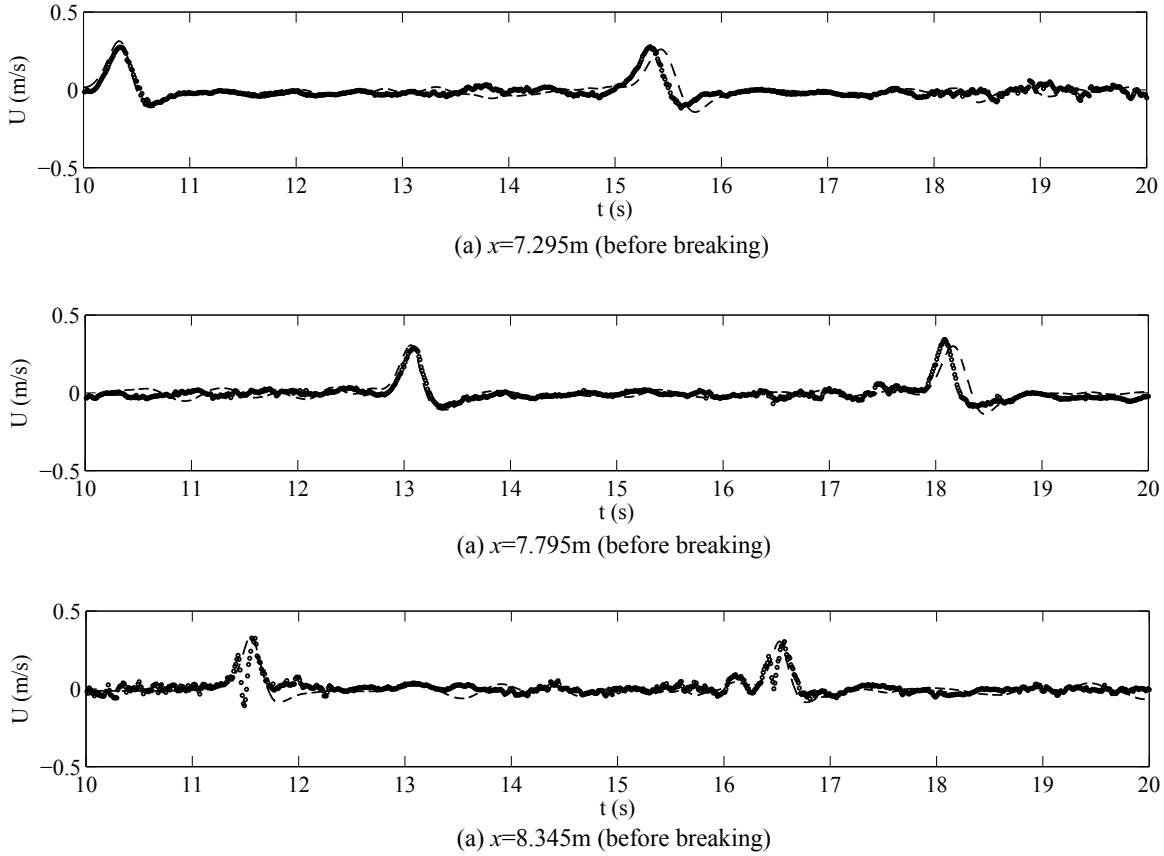

Figure 19: Comparison of numerical and experimental vertical velocity for the plunging breaker. Dashed lines: present numerical results; circles/full line: experimental results by **?**

21 (c). This is consistent with the previous studies by **?** and **?**. Moreover, the computed horizontal and vertical velocity for both cases are consistent with the laboratory measurements by **??**.

4.3.4 Variation of time-mean turbulent kinetic energy

Fig. 22 shows the comparison of computed and measured square root of the non-dimensional time-mean turbulent kinetic energy versus the non-dimensional water depth after the breaking point at x=6.665m, 7.275m and 7.885m for the spilling breaker. The numerical results of **??** are also presented for comparison as reported in **?**. It appears that the variation of time-mean turbulent kinetic energy with the water depth increases gradually as the distance to the free surface decreases. The present numerical results at x=6.665m is compared only with the numerical results by **?** as the experimental data is not available. It is observed that the computed results by **?** are slightly larger than the experimental measurements at x=7.275m, but they are in good agreement at x=7.885m. The computed results by **?** show a significant underestimation of turbulence intensity at x=7.275m. With the present numerical model, the variation of turbulence intensity is well represented at x=7.275m but it is slightly

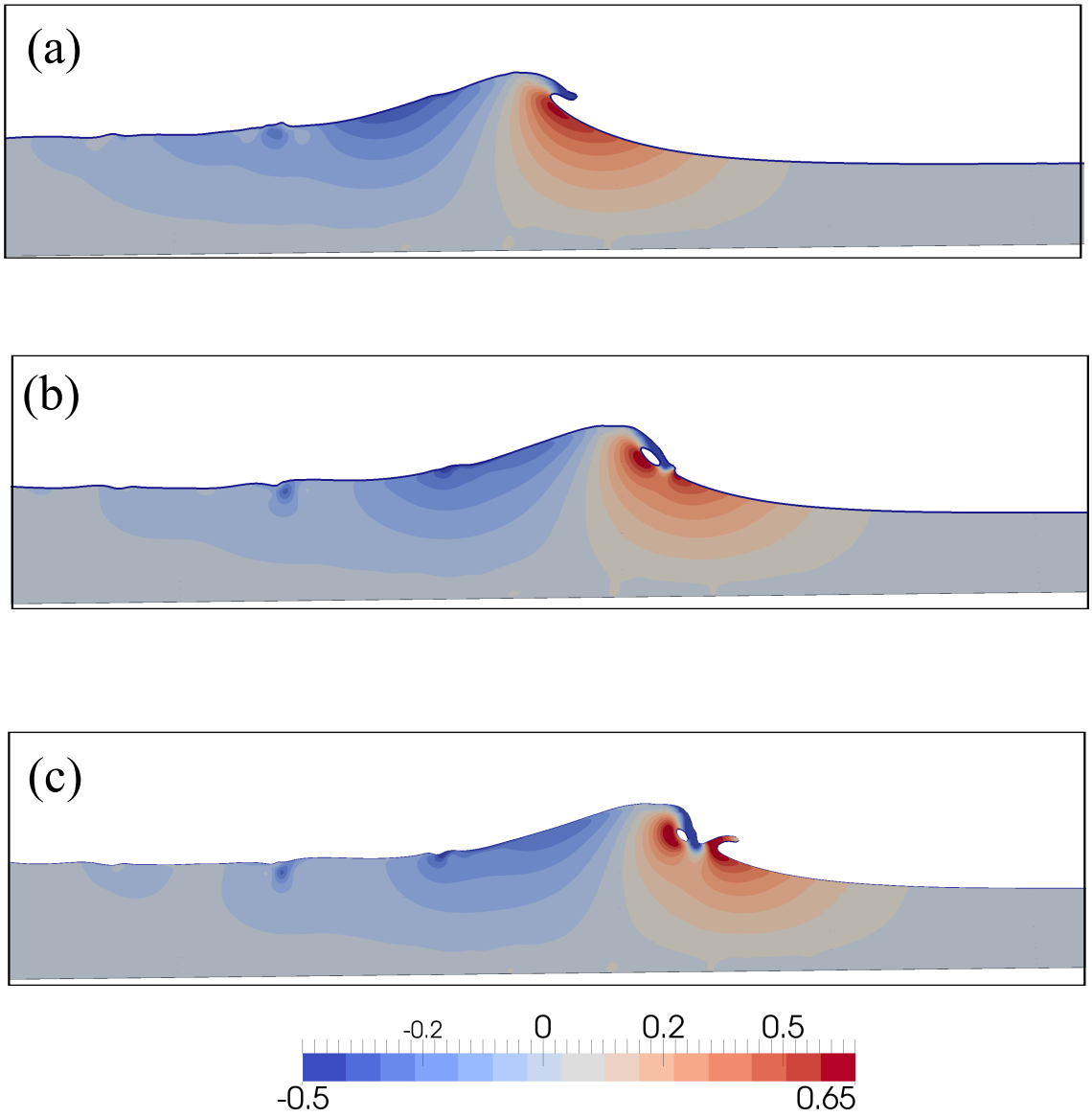

Figure 20: Variation of vertical velocity, V_z (m/s) under the spilling breaker at t= 10.35s (a), 10.45s (b) and 10.50s (c)

underestimated at x=7.885m.
Fig. 23 shows the comparison of computed and measured square root of the non-dimensional time-mean turbulent kinetic energy versus the non-dimensional water depth after the breaking point at x=8.345m, 8.795m and 9.295m for the plunging breaker. The predicted turbulence intensity profile by **?** agrees well with the experimental data at x=8.345m and 8.795m, though this is overestimated slightly at x=9.295m. The results by **?** also show a good prediction at x=8.345m. Though the present numerical model represents the vertical turbulence

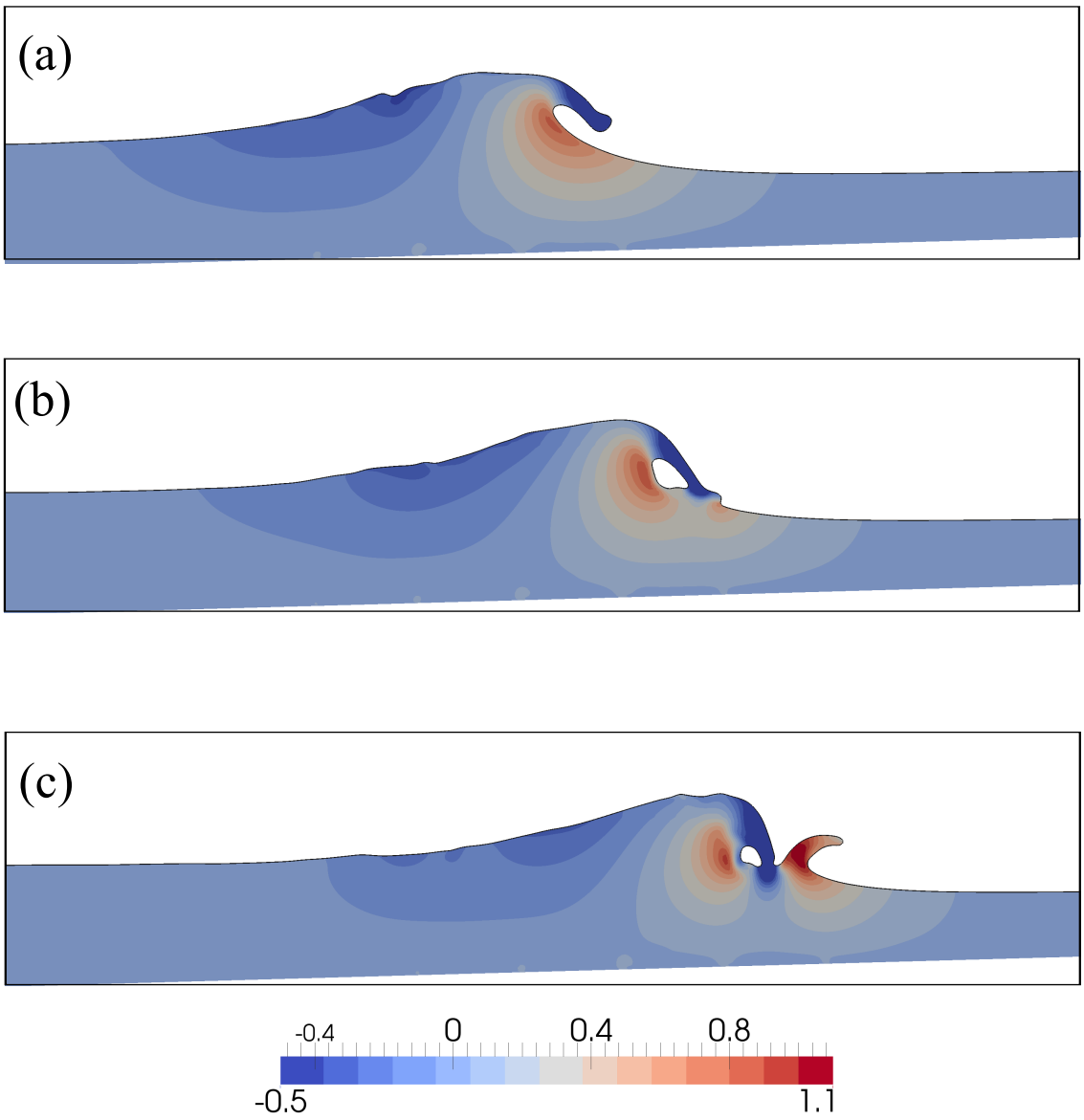

Figure 21: Variation of vertical velocity, V_z (m/s) under the plunging breaker at t= 10.85s (a), 10.95s (b) and 11.05s (c)

profile quiet well at x=8.345m, the model slightly underestimates the profile at x=8.795m and 9.295m. For both cases, the turbulence is generated after the wave breaking when the flow characteristics change significantly leading to the formation of the surface roller. The turbulence intensity increases gradually shoreward until the surface roller dissipates energy completely during the transformation in the surf zone. In addition, the maximum value of the turbulence intensity occurs near the free surface and decreases gradually with the water depth. It is observed that the turbulence intensity generated by the plunging breaker is much

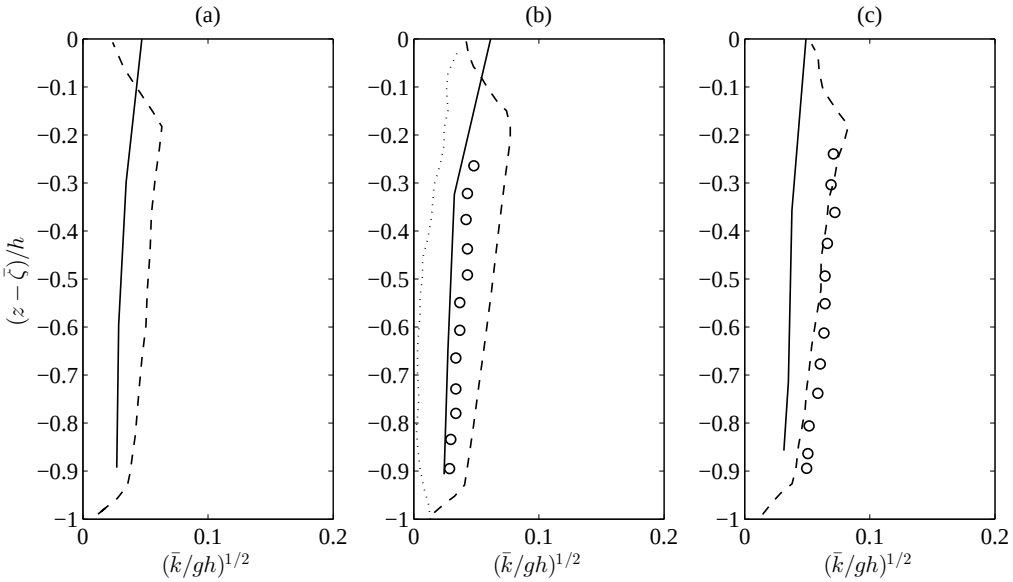

Figure 22: Comparison of the computed and measured square root of the non-dimensional time-mean turbulent kinetic energy versus the non-dimensional water depth at x=6.665m (a), 7.275m (b) and 7.885m (c) for the spilling breaker. Solid lines: the present numerical model; circles: experimental data from Ting and Kirby (1995); dotted lines, numerical: Bradford (2000); dashed lines, numerical: Xie (2013)

stronger than for the spilling breaker, being consistent with **?**.
Overall, the present numerical results are in reasonable agreement with the measured data and the other numerical models. However, the model underestimates the vertical turbulence profile in the surf zone. The detailed investigation on the turbulence characteristics in the surf zone is not considered in present study. In fact, the modelling of the complex turbulent characteristics in the surf zone necessitates the use of more sophisticated turbulence modelling techniques. In addition, these simulations are computationally demanding. Further development of the current numerical model concerning the turbulence modelling is required to capture the detailed surf zone hydrodynamics.

4.3.5 Transformation of free surface profile

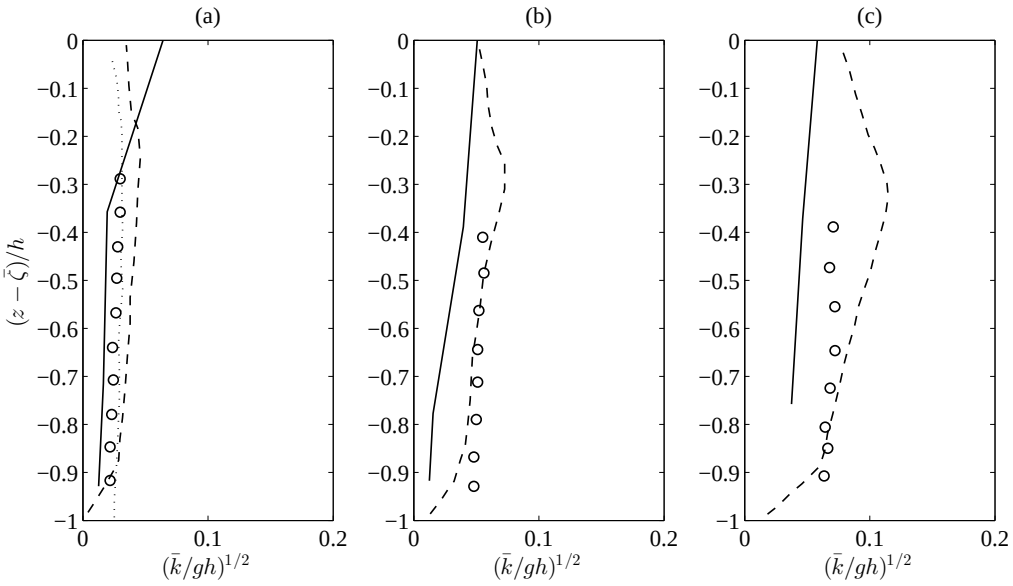

Figure 23: Comparison of the computed and measured square root of the non-dimensional time-mean turbulent kinetic energy versus the non-dimensional water depth at x=8.345m (a), 8.795m (b) and 9.295m (c) for the plunging breaker. Solid lines: the present numerical model; circles: experimental data from Ting and Kirby (1995); dotted lines, numerical: Bradford (2000); dashed lines, numerical: Xie (2013)

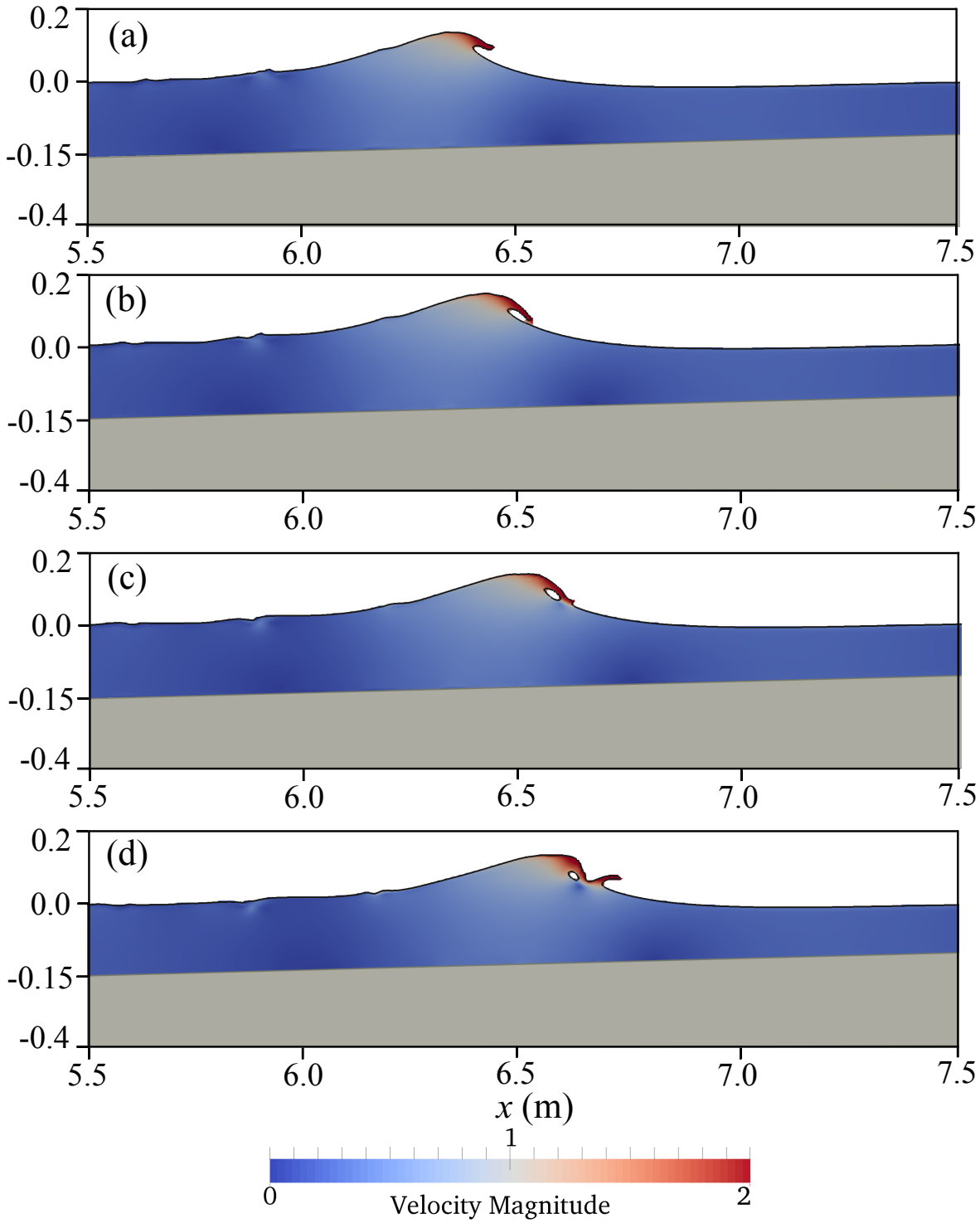

Figure 24: Simulated velocity variation (m/s) and free surface profile changes during the breaking process at t= 10.35s (a), 10.40s (b), 10.45s (c) and 10.50s (d) for the spilling breaker

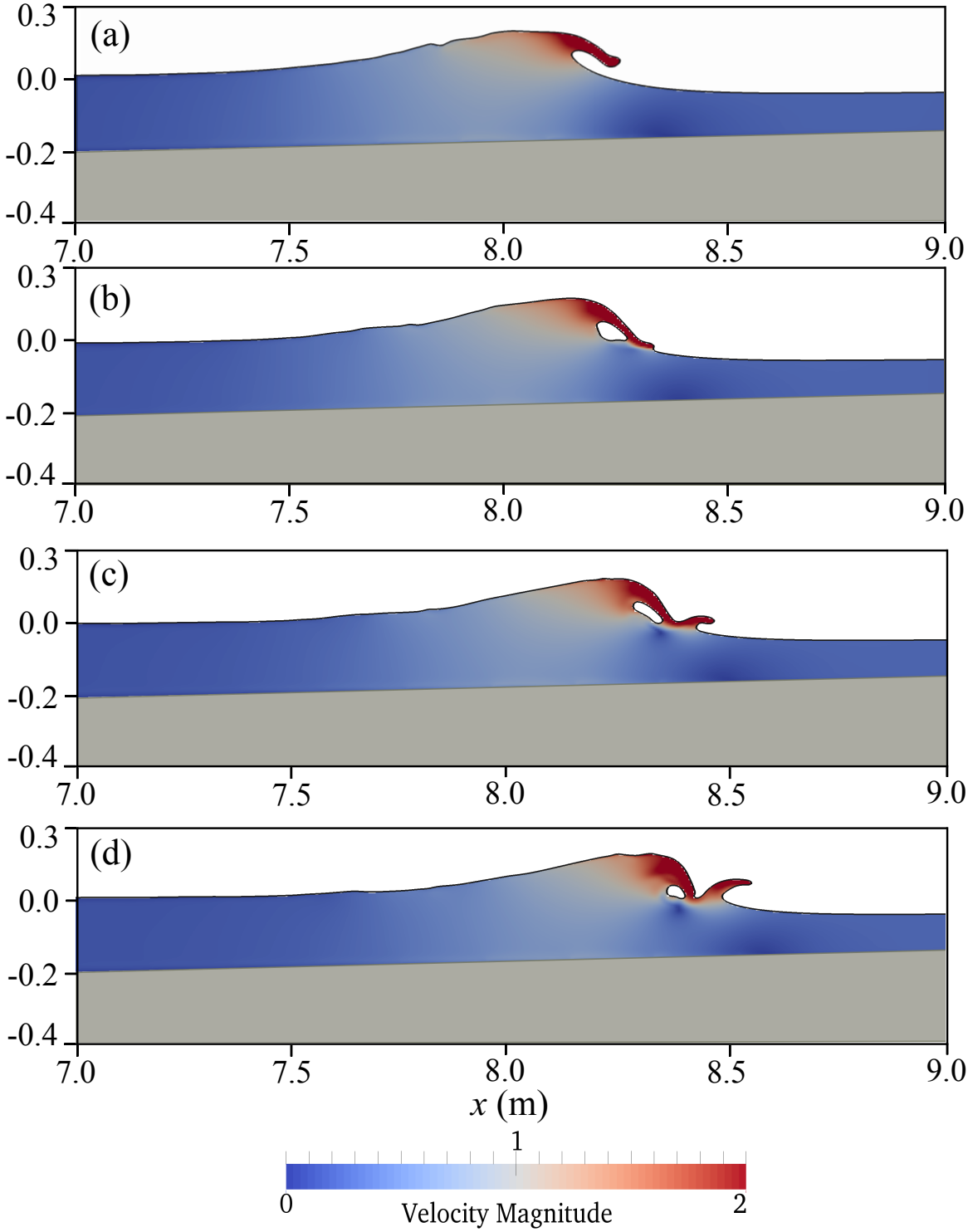

Figure 25: Simulated velocity variation (m/s) and free surface profile changes during the breaking process at t= 10.85s (a), 10.95s (b), 11.00s (c) and 11.05s (d) for the plunging breaker

Figs. 24 and 25 show he transformation of the free surface profile during the breaking process for spilling and plunging breakers, respectively. It appears that the forward overturning wave crest during the breaking process moves faster than the lower part of the wave with high crest velocity (Figs. 24 (a) and 25 (a)). Thus, the overturning water jet falls onto the free surface as it propagates over the slope, as seen in Fig. 24 (c) and 25 (b). When the water jet plunges down on the trough of the preceding wave, a rotating motion with an air pocket inside and a surface roller are created by a combination of the downstream return flow under the preceding wave trough together with the overturning jet and the forward motion of the wave crest. The size of the rotating plunger motion is similar to the initial plunger vortex as shown in Fig. 1. Further, a portion of water which is equivalent to the strength of the jet is displaced and pushed forward during the impact of the overturning water jet on the free surface and creates a secondary wave in the surf zone as depicted in Figs. 24 (d) and 25 (c) and (d). Therefore, the main sources of turbulence for the plunging wave are the transformation of rotational motion and the surface roller (**??**). The present study shows that both spilling and plunging breakers are found to have similar flow features during the initial breaking process. This has been confirmed experimentally by **??**. The authors also addressed that in spite of similar flow features between plunging and spilling breakers, turbulent generating mechanism and their characteristics are different.

4.3.6 Wave profile asymmetry properties

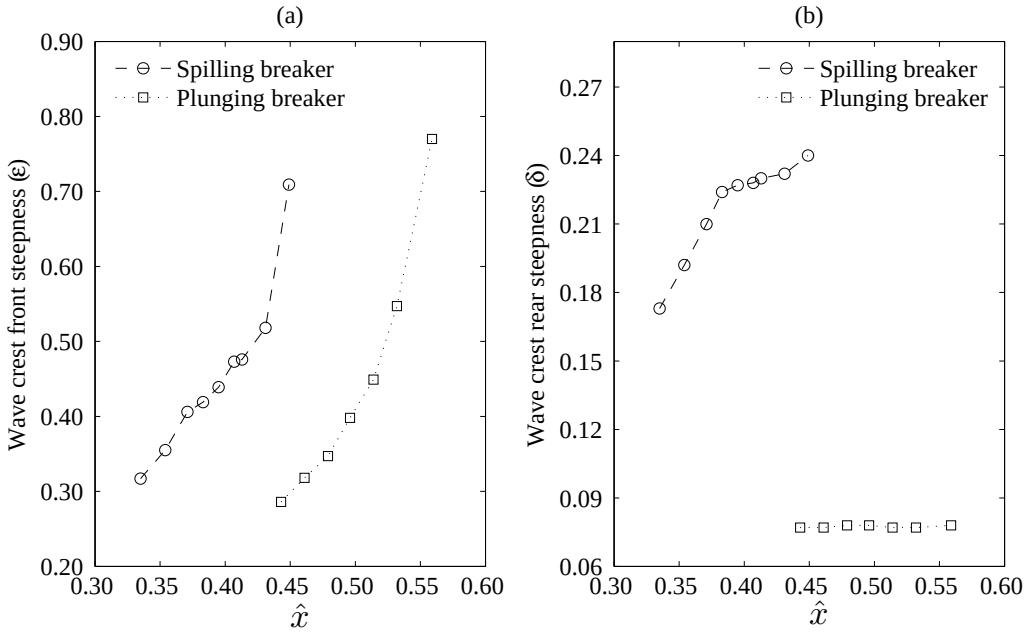

Figure 26: Simulated development of steepness parameters (a) wave crest front steepness (ε); (b) wave crest rear steepness (δ) versus the non-dimensional breaking location ($\hat{x}$) during the transition to breaking

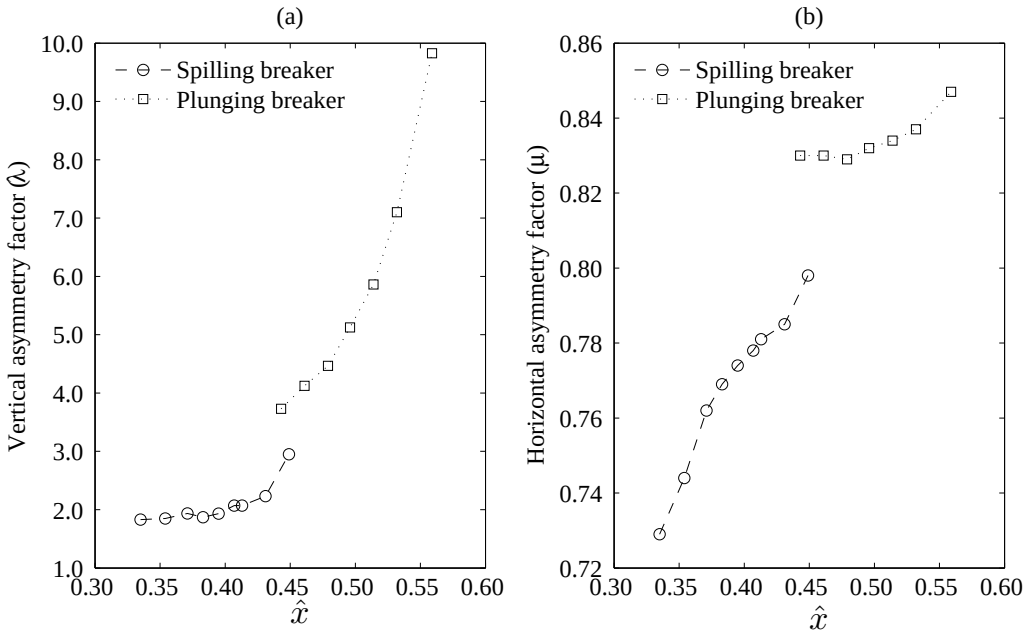

Figure 27: Simulated development of asymmetry factors (a) vertical asymmetry factor (λ); (b) horizontal asymmetry factor (μ) versus the non-dimensional breaking location ($\hat{x}$) during the transition to breaking

Now the steepness and asymmetry parameters defined by **?** are used to describe the geometric properties of the wave profile asymmetry during breaking. In order to investigate the geometric properties of a wave approaching breaking, the steepness and asymmetry parameters of each wave are calculated at different locations along the wave tank until the breaking point.

Fig. 26 shows the variation of the wave crest front steepness (ε) and the wave crest rear steepness (δ) for the spilling and plunging breakers. It appears that ε increases as the wave approaches breaking in both cases; the front face of the wave becomes steeper for the plunging breaker than for the spilling breaker (Fig. 26(a)). On the other hand, δ increases as the wave approaches the breaking point for the spilling breaker, whereas it does not change during the transition stage for the plunging breaker. Fig. 27 shows the vertical asymmetry factor (λ) and the horizontal asymmetry factor (μ) for the spilling and plunging breakers. It appears that λ and μ increase as the wave approaches breaking for both cases. However, λ increases rapidly and μ increases slowly for the plunging breaker, while λ increases slowly and μ increases rapidly for the spilling breaker. For the spilling breaker, the front and rear face of the wave crest become steeper with a gradual increase of the vertical asymmetry, and the forward wave trough flattens as the wave approaches breaking. For the plunging breaker, the front face of the wave crest becomes very steep without much change in the rear face of the wave crest. The vertical asymmetry becomes larger with small changes in the preceding wave trough. The computed trend of the steepness and asymmetry parameters of waves close to breaking over the slope is consistent with the results from the experimental studies of deep water waves by **?** and **?**.

5 Conclusions

The two-phase flow model REEF3D has been used to model waves breaking over a sloping seabed. The Reynolds-Averaged Navier-Stokes (RANS) equations are solved together with the level set method (LSM) for the free surface and the $k-\omega$ turbulence model. Numerical experiments are performed in order to investigate the hydrodynamic characteristics and geometric properties of plunging breakers over slopes. Comparison with similar results obtained for spilling breakers in **?** are also discussed. The results show that the numerical model is capable of describing the prominent physical flow characteristics such as the formation of forward overturning water jet, air pocket, splash-up, and the secondary wave during the breaking process. The numerical model shows a good match with the measurements by **??** for the free surface elevation, horizontal and vertical particle velocities. The hydrodynamic characteristics of spilling and plunging breakers in terms of the wave height evolution and attenuation, horizontal and vertical velocity components, free surface profile evolution, and the geometric properties during the development of the breaking process are presented and discussed. This knowledge allows to learn and to understand more about the physical processes related to wave breaking. This will in turn improve the assessment of the hydrodynamic loads on offshore and coastal structures and the flow characteristics around them. The following main conclusions can be drawn from the numerical investigations:

- The variation of the breaker depth index (γ_b) of plunging breakers over slopes shows a similar trend as for the spilling breakers. On the other hand, the breaker height index (Ω_b) varies opposite to the trend of the spilling breakers, i.e. the breaker height index (Ω_b) increases as the slope becomes steeper. The breaker indices for the plunging breakers over a given slope for different offshore wave steepness (H_0/L_0) are consistent with the spilling breakers.

- For both spilling and plunging breakers over slopes, the wave profile asymmetry properties at the breaking point are found to be similar for the crest front steepness (ε), vertical asymmetry factor (λ) and horizontal asymmetry factor (μ), but different for the crest rear steepness (δ). The rear part of the wave crest of the plunging breakers does not change much during the interaction with slopes, while it does for spilling breakers.

- The crest front steepness (ε) increases and vertical asymmetry factor (λ) decreases as the offshore wave steepness (H_0/L_0) increases for plunging breakers which is consistent with that of spilling breakers. However, the crest rear steepness (δ) and horizontal asymmetry factor (μ) are almost independent of offshore wave steepness (H_0/L_0) for plunging breakers.

- Unlike spilling breakers over slopes, the wave profile asymmetry properties of plunging breakers, except the vertical asymmetry factor (λ), are less dependent on the seabed slope and the offshore wave steepness (H_0/L_0).

- The wave undergoes more deformation for the plunging breaker than for the spilling breaker as it breaks at a shallower water depth with a larger breaker height. Therefore, the wave height to water depth ratio H/d is larger for the plunging breaker than for the spilling breaker.

- The change in the initial wave characteristics of the wave approaching the breaking point is larger for the plunging breaker as it has a deeper wave base and experiences higher shoaling rate than for the spilling breaker.
- A rapid transition of the wave height occurs after breaking in the surf zone for the plunging breaker, while it is more gradual for the spilling breaker.
- The variation of the horizontal velocity component below the wave trough is almost constant over the water depth for the plunging breaker, while it is significant under the spilling breaker. It is noticed that the maximum horizontal velocity component occurs at the tip of the main wave crest and the secondary wave crest.
- For both spilling and plunging breakers, the maximum vertical particle velocity component becomes larger under the steep wave front. Although the kinematics of the main wave crest and the secondary wave crest are dominated by the horizontal velocity component, the vertical velocity component has a significant contribution in the formation of the secondary wave during splash-up.
- For spilling and plunging breakers, the physical flow process is found to have similar features such as the formation of a forward overturning water jet, air entrainment, splash-up, and the secondary wave during the breaking.
- For the spilling breaker, the wave crest becomes narrower with steeper wave front face and rear face and the wave trough depth flattens as the wave approaches breaking. For the plunging breaker, the wave crest becomes wider with steeper wave front face and broader rear face and small changes in the wave trough depth during the transition to breaking.

Acknowledgment

The authors would like to thank Dr. James Kirby and Dr. Ting Francis for sharing the experimental data. The work was supported by the Norwegian Research Center for Offshore Wind Technology (NOWITECH), Research Council of Norway (Contract no.193823). The authors would also like to thank NOTUR (Project no. NN9240K) for allocation of computational resources provided on the Vilje system at the super computing facilities at NTNU.